nuclear fusion
IAEA

PAPER • OPEN ACCESS

SOLPS-ITER modeling of neon-seeded EAST plasmas under connected double-null configurations and its impact on tungsten impurity behaviors

To cite this article: Fuqiong Wang *et al* 2026 *Nucl. Fusion* **66** 016037

OPEN ACCESS
IOP Publishing | International Atomic Energy Agency
Nuclear Fusion
Nucl. Fusion **66** (2026) 016037 (26pp)
https://doi.org/10.1088/1741-4326/ae1f9e

SOLPS-ITER modeling of neon-seeded EAST plasmas under connected double-null configurations and its impact on tungsten impurity behaviors

Fuqiong Wang[1,2,*], R. Yan[3,*], Y.F. Xu[1,2], S.C. Liu[1,2], X.J. Zha[1,2], F.C. Zhong[1,2], Y. Liang[4], S.T. Mao[3], Y.M. Duan[3] and L.Q. Hu[3]

[1] College of Physics, Donghua University, Shanghai 201620, China
[2] Member of Magnetic Confinement Fusion Research Center, Ministry of Education, Shanghai, China
[3] Institute of Plasma Physics, Chinese Academy of Sciences, Hefei 230031 Anhui, China
[4] Forschungszentrum Jülich GmbH, Institut für Energie- und Klimaforschung Plasmaphysik, Jülich, Germany

E-mail: wangfq@dhu.edu.cn and yanrong@ipp.ac.cn

Received 30 July 2025, revised 7 October 2025
Accepted for publication 14 November 2025
Published 26 November 2025

Abstract

The SOLPS-ITER edge modeling package was employed to numerically investigate neon (Ne)-seeded EAST plasmas under connected-double-null configurations, focusing on Ne impurity transport and its impacts on tungsten (W) impurity behaviors. Results reveal that $\boldsymbol{E} \times \boldsymbol{B}$ drift significantly modifies the target profiles of plasma density (n_e) and temperature (T_e) by modulating divertor particle transport, thereby strongly influencing W sputtering. Without drifts, radial particle transport into the far divertor SOL is minimal, resulting in low n_e and high T_e, which in turn leads to significant W sputtering in this region. Drifts shift the peak positions of n_e and T_e at the target, and generate significant in-out/up-down divertor asymmetries. Notably, in-out divertor asymmetry in T_e exhibits a distinct dependence on Ne puffing rate ($\Gamma_{\mathrm{Ne,puff}}$) compared to single-null configurations. W sputtering can be effectively reduced by increasing $\Gamma_{\mathrm{Ne,puff}}$, but only when radial particle transport into the far divertor SOL is significantly enhanced by $\boldsymbol{E} \times \boldsymbol{B}$ drift. Under drift-free conditions, low $\Gamma_{\mathrm{Ne,puff}}$ leads to stagnation points for the poloidal Ne (W) velocity within divertor regions, causing a significant Ne (W) divertor leakage through the near SOL. This leakage can be alleviated by increasing $\Gamma_{\mathrm{Ne,puff}}$. Conversely, at high $\Gamma_{\mathrm{Ne,puff}}$, influences of Ne on the deuterium ionization source in the divertor regions leads to the redistribution of Ne density from the upper to lower divertor through the main SOL. In full-drift scenarios, the $\boldsymbol{E} \times \boldsymbol{B}$ drift dominates the poloidal flow of Ne and W, as in single-null plasmas, but the stagnation point and divertor retention are less

* Authors to whom any correspondence should be addressed.

sensitive to $\Gamma_{\mathrm{Ne,puff}}$ variations in CDN configurations. Neglecting drifts leads to a substantial overestimation of Ne and W densities near the core boundary. The differing spatial distribution of Ne^{+} and W^{+} ionization sources from neutrals leads to distinct ion flux patterns for Ne and W. Importantly, increasing $\Gamma_{\mathrm{Ne,puff}}$ can reduce W core leakage.

Keywords: EAST, edge plasma, impurity seeding, impurity transport, W sputtering, drifts, divertor retention

(Some figures may appear in colour only in the online journal)

1. Introduction

In high-power tokamak operations, the effective management and dissipation of the substantial power flux traversing the separatrix from the core plasma into the scrape-off layer (SOL) [1] prior to reaching the divertor plates is of critical importance. Failure to achieve this would likely result in the exceeding of the anticipated stationary material limits of $5-10$ MW m^{-2} for the perpendicular target heat fluxes and 5 eV for the target plasma temperatures, potentially causing severe damage to plasma-facing components (PFCs) and significant erosion of the target material [2–7]. A widely adopted strategy to mitigate divertor heat loads is impurity seeding, which enhances radiative power dissipation and redistributes energy over a larger area than the plasma-wetted zone on the target plates. In tokamaks with full metal walls, such as ITER [8] and DEMO [9], the introduction of extrinsic impurities is essential for addressing the challenges of power exhaust.

Noble gases, such as neon (Ne), which exhibit minimal surface chemistry, are currently the primary candidates for acting as key radiators in this process. Although sufficient impurity seeding can maintain divertor heat loads at manageable levels, an excessive influx of seeded impurities into the core plasma can degrade confinement performance and potentially lead to radiation-induced plasma collapse. Moreover, impurity seeding significantly contributes to the erosion of PFC materials [10], particularly tungsten (W), which is the primary candidate for the divertor target plate. This is attributed to the higher bombardment energy and lower sputtering threshold energy of the injected impurities compared to background plasma ions. Recent investigations have also revealed that seeded Ne impurities significantly affect W divertor leakage [11], thereby greatly influencing W plasma content, which should be strictly controlled (e.g. below 10^{-5} in ITER [12]). To realize a viable fusion power energy source in the future, it is imperative to achieve a comprehensive and nuanced understanding of the behavior of seeded impurities, as well as their multifaceted influences on the behavior of W impurities.

Another effective strategy for mitigating divertor heat loads involves increasing the plasma-wetted area through geometric techniques. These techniques include tilting target plates and employing advanced magnetic divertor configurations, such as the snowflake [13, 14] and super-X [15] divertors. Double-null (DN) magnetic configurations offer significant advantages over conventional single-null (SN) designs by enhancing energy dissipation through geometric redistribution in tokamaks [16–18]. Moreover, DN configurations improve the symmetry of power heat load distribution on divertor target plates, which is directly linked to enhanced plasma confinement performance. As a result, the DN configuration is considered a promising option for future fusion reactors, such as the European DEMO [19].

The EAST tokamak [20], a fully superconducting device designed for long-pulse operations with high heating power, can address power and particle challenges comparable to those in ITER, with steady-state heat fluxes reaching approximately 10 MW m^{-2}. In pursuit of more ambitious scientific objectives, the EAST tokamak has progressively upgraded its machine configuration and is transitioning to a full metal wall. Currently, two ITER-like W divertors with distinct geometries are installed at the top and bottom of EAST [21]. Impurity seeding is routinely employed on EAST to mitigate divertor heat loads, and recent experiments have successfully demonstrated stable Ne-seeded H-mode regimes [22]. Additionally, EAST uniquely supports flexible operation in both upper/lower single null (USN/LSN) and double null (DN) configurations.

Recent advancements in research on EAST have seen a surge in simulation studies focusing on impurity-seeded plasmas, particularly those involving Ne [23] and argon (Ar) [24], as well as the behavior of W [25–29] impurities within these plasmas. Despite the valuable insights gained from these studies, most prior simulations have been confined to upper or lower single-null plasma configurations. This limitation has restricted the comprehensive understanding of impurity transport and interactions in more complex plasma geometries. To address this gap, the present study employs the comprehensive SOLPS-ITER code [30, 31] to numerically investigate the transport properties of Ne impurities and systematically evaluate their effects on W impurity behavior in the EAST tokamak plasmas, specifically focusing on configurations with connected double-null (CDN) divertors. Previous simulation studies have shown that electric and diamagnetic drifts are crucial factors influencing divertor asymmetry [32] and leakage of both low- [33] and high-Z [34, 35] impurities in tokamak plasmas. Therefore, these effects are incorporated into our current simulation.

The remainder of this paper is organized as follows: section 2 details the numerical framework and simulation setup. Section 3 presents a comprehensive analysis of the results, beginning with an examination of Ne-seeded plasma characteristics (section 3.1), followed by the transport property

of Ne impurity (section 3.2) and a systematic exploration of Ne-induced modifications to the production and transport of W impurity (section 3.3). Finally, section 4 summarizes the principal findings and their implications for managing plasma-wall interactions in magnetic confinement devices.

2. Simulation setups

The simulation work was conducted using the SOLPS-ITER code [30, 31], a comprehensive numerical tool designed to model the intricate physical processes occurring in the edge of tokamak plasmas. The SOLPS-ITER code integrates a two-dimensional fluid code B2.5 [36] and a three-dimensional Monte Carlo code EIRENE [37]. The B2.5 code is constructed based on the drift-reduced Braginsky equations and includes a self-consistent model for electric and diamagnetic drifts, plasma currents, and electrostatic potential [38]. The EIRENE kinetic code is employed to account for neutral atoms and molecules. It provides the particle, momentum, and energy sources and sinks associated with molecular-atomic processes, which are essential for the plasma fluid equations. The neutral viscosity due to nonlinear neutral-neutral collisions are added through the BGK approach.

The physical meshes utilized for SOLPS-ITER simulations are depicted in figure 1(*a*). These meshes are composed of quasi-orthogonal grids for the B2.5 code (consisting of 96 poloidal $\times$ 36 radial cells, aligned along the magnetic flux surfaces) and triangular grids for the EIRENE code. These meshes were generated based on a generic magnetic equilibrium in EAST, featuring a CDN plasma configuration with the following parameters: elongation $\kappa = 1.781$, upper/lower triangularity $\delta_u/\delta_l = 0.590/0.586$, safety factor at the 95% flux surface $q_{95} = 5.0$, plasma current $I_p = 400$ kA, and toroidal magnetic field $B_T = 2.435$ T. At the outboard midplane (OMP), the B2.5 meshes radially extend from -5.9 cm (core) to approximately 2.8 cm (SOL). At the inner midplane (IMP), they extend from -10.0 cm (core) to approximately 3.5 cm (SOL). To facilitate the analysis, the calculation regions, including the 'core', the main SOL (excluding the divertor regions), and the four (lower-inner (LI), upper-inner (UI), upper-outer (UO) and lower outer (LO)) divertor regions, as well as the computational meshes are highlighted in figure 1(*b*).

To examine the impact of drift effects on the up-down divertor asymmetry in EAST with its upgraded device configuration, Ne impurity gas was introduced via a wall element located at the OMP ($Z = 0$, see figure 1(*a*)). This approach was employed to avoid the introduction of artificial up-down asymmetry. Three distinct scenarios are simulated: (1) no ion drifts, (2) full ion drifts with a downward $\mathbf{B}\times\nabla$B direction ($\mathbf{B}\times\nabla$B$\downarrow$), and (3) full ion drifts with an upward $\mathbf{B}\times\nabla$B direction ($\mathbf{B}\times\nabla$B$\uparrow$). The typical drift flow patterns of plasma ions for scenario (2) and that for scenario (3) are depicted in figures 2(*a*) and (*b*), respectively. In each scenario, the Ne puffing rate has been varied from 1.0 to 15.0 $\times$ 10^{19} Ne atoms/s. W impurities were assumed to be generated by physical sputtering due to the bombardment of deuterium (D) and Ne species at the target plates. Additionally, self-sputtering of W impurities was also considered. The sputtering yield of W impurities was calculated using the modified Roth-Bohdansky model [39]. Consistent with previous work [26], an average incident angle of 45° was assumed in the calculations. The redeposition rate of W was specified as 0.9.

Details on the considered neutral and fluid species are listed in table 1. In B2.5 simulations, electrons (e^-) and each charge state of fuel and impurity species are typically treated as distinct fluids. However, the increased number of fluid equations significantly raises the computational cost and numerical instability. Therefore, in our simulation, the 74 W ion charge states were bundled into 23 fluid species, referred to as the 'jett' bundle model (table 1). The 'jett' model is capable of effectively treating low-charge-state W ions and accurately calculating core radiation [40]. Impurity interactions were simulated using the standard SOLPS-ITER model, with thermal and friction coefficients derived from the Zhdanov–Yushmanov expressions [41, 42]. The new Zhdanov closure scheme [43–45] was not employed in this work; its potential implications will be explored in future studies.

In SOLPS-ITER simulations, the plasma conditions at the boundaries of the computational grid for B2.5 must be specified. These boundaries include the core boundary, the target plates, the outermost ring in the private flux region (PFR), and the outermost ring in the SOL. Although the fixed D^+ ion flux condition at the core boundary may more closely approximate experimental conditions, the fixed core density approach is generally favored for its enhanced numerical stability and greater ease in achieving convergence, particularly in simulations that include drift effects [46]. Therefore, in this study, the plasma ion (D^+) density at the core boundary is set to a constant value of $n_u = 3.5 \times 10^{19}$ m^{-3}. The net flows of charged neon (Ne) and tungsten (W) species from the core are set to zero. The total power entering the computational domain through the core boundary is 3.6 MW, equally split between ions and electrons. Since the neutral deuterium (D^0), neon (Ne^0) and tungsten (W^0) species are treated by EIRENE (table 1), boundary conditions for them on the B2.5 side are unimportant. On the EIRENE side, the core boundary is assumed to absorb all the neutrals impinging from the outer side. At the far SOL and PFR, leakage-type boundary conditions are applied for ion density and energy balances. It is assumed that the radial flow of ions (Γ_l), ion energy ($q_{l,i}$) and electron energy ($q_{l,e}$) across the outer boundary of SOL and PFR are proportional to local sound speed: $\Gamma_l = \delta_n n_i c_s$, $q_{l,i} = \delta_i n_i c_s T_i$, $q_{l,e} = \delta_e n_e c_e T_e$. Where $c_e = \sqrt{T_e/m_e}$, $c_s = \sqrt{(T_e + T_i)/m_i}$ and the leakage coefficients are $\delta_n = 1.0 \cdot 10^{-3}$, $\delta_i = 1.0 \cdot 10^{-2}$, $\delta_e = 1.0 \cdot 10^{-4}$. At the divertor target plates the standard sheath boundary condition is used; the plasma flow is assumed to be at least sonic at entrance of sheath, i.e. $n\frac{B_\theta}{B}V_{\|} = n\frac{B_\theta}{B}c_s$. Here, B_θ /B and n

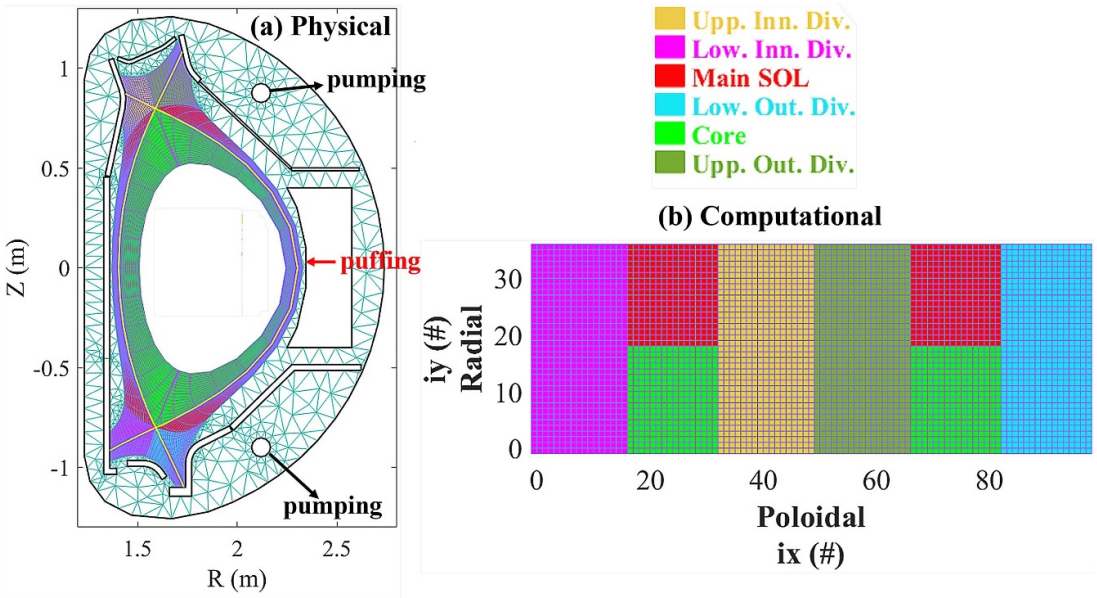

Figure 1. (*a*) The physical meshes for B2.5 (quasi-orthogonal meshes poloidally aligned along the flux surfaces) and for EIRENE (triangular) as well as (*b*) the computational meshes for B2.5. The in-vessel structures as well as the pumping and puffing locations are also shown.

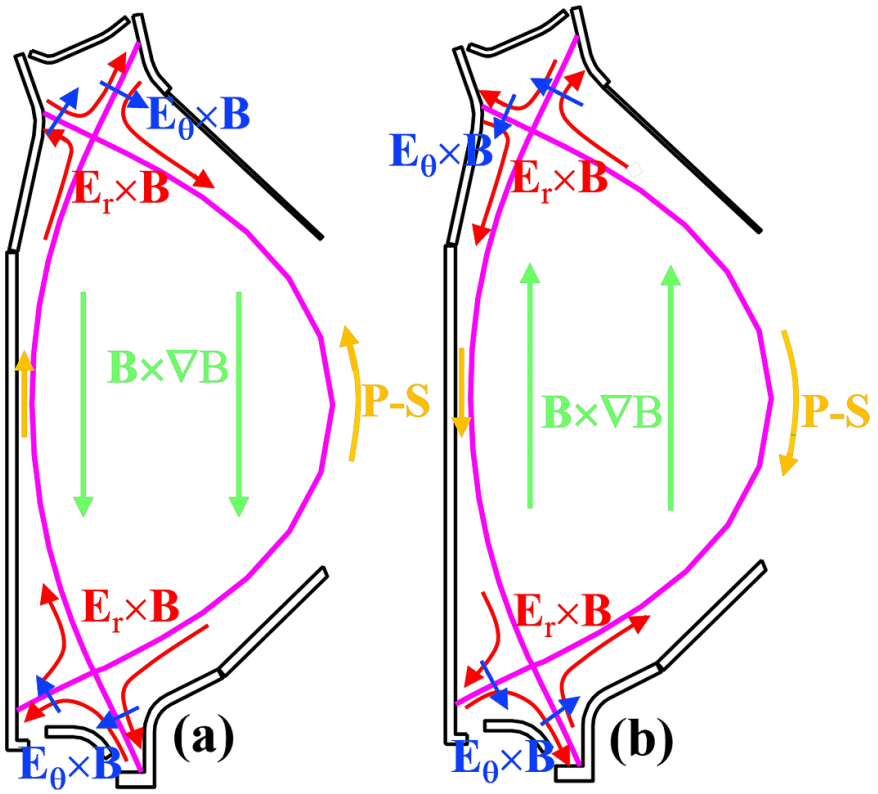

Figure 2. Typical drift flow patterns of ions in EAST plasmas under the connected double null (CDN) configuration for downward (*a*) and upward (*b*) ion $\boldsymbol{B}\times\nabla B$ drift.

Table 1. The considered neutral and fluid species. The full 74 charge states for W are bundled to 23 fluid species.

	B2.5	EIRENE
D	D^+, e^-	D^0, D_2, D_2^+
Ne	Ne^+, Ne^{2+}, Ne^{3+}, Ne^{4+}, Ne^{5+}, Ne^{6+}, Ne^{7+}, Ne^{8+}, Ne^{9+}, Ne^{10+}	Ne^0
W	W^{1+}, W^{2-4+}, W^{5+}, W^{6+}, W^{7+}, W^{8+}, W^{9+}, W^{10-12+}, W^{13-16+}, W^{17+}, W^{18+}, W^{19+}, W^{20+}, W^{21-22+}, W^{23-25+}, W^{26-27+}, W^{28-29+}, W^{30-31+}, W^{32-33+}, W^{34-40+}, W^{41-45+}, W^{46-55+}, W^{56-74+}	W^0

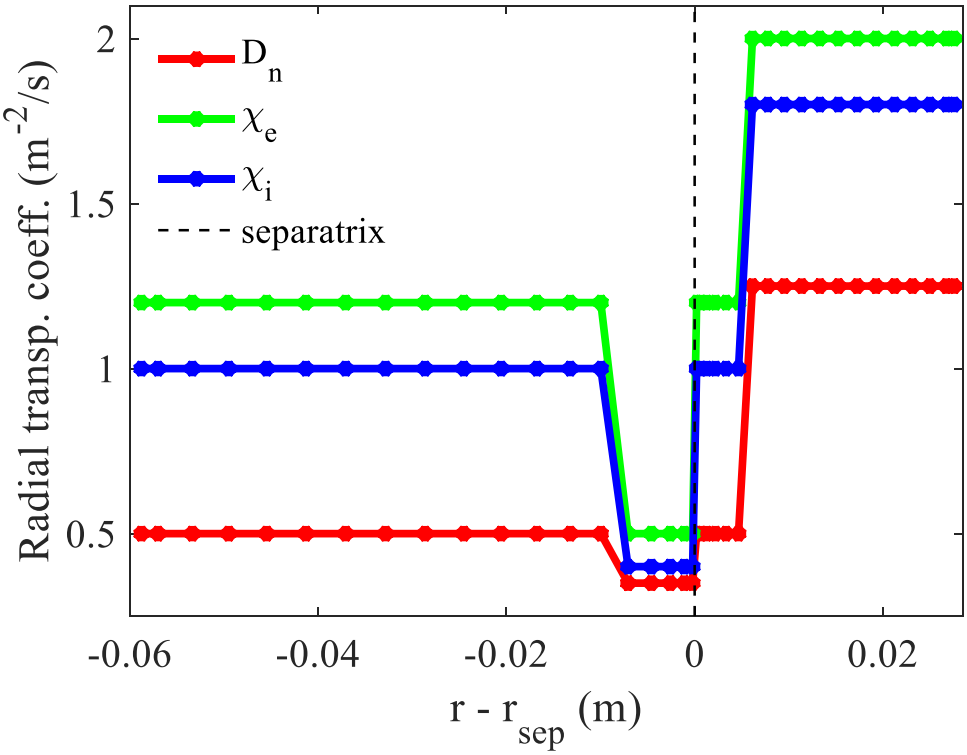

Figure 3. Radial transport coefficients plotted against distances to the separatrix at the equatorial midplane, low field side (LFS). Positive abscissa values correspond to SOL, negative values to the core.

denote the parallel plasma flow velocity, poloidal/total magnetic field, and plasma density, respectively. In the full-drifts simulation cases, boundary conditions at the targets are revised as:, where V_p represents the poloidal projection of total drift velocities [32].

The recycling coefficient (R) at the surfaces of PFCs is specified as follows: R is set to 1.0 for divertor plates and for the main chamber. For the two pumping holes, each with a surface area of 2.087 m^2 (figure 1(a)), R is set to 0.9152. This configuration results in a pumping speed of approximately 2×76 $m^3 \cdot s^{-1}$, which is consistent with the typical pumping capability of the cryopump in EAST [47, 48]. The radial particle and thermal transport coefficients are specified based on typical values observed in H-mode plasmas in EAST, as referenced from prior simulation studies [49] (figure 3). The radial diffusivity profiles shown in figure 3 are applied uniformly in the poloidal direction. Only steady-state discharges are simulated; transient events, such as edge-localized modes (ELMs), are not considered. Typically, in H-modes, the plasma exhibits long mean-free paths and/or short local gradient scale lengths of plasma parameters relative to characteristic plasma scales, necessitating the use of flux limiters to account for kinetic effects within the fluid framework [1, 50, 51]. Such limiters constrain both electron and ion parallel heat conduction, as well as ion momentum flux (viscosity), to fractions of their convective free-streaming limits. For our simulations, electron and ion heat flux limiters are set to 0.3 and 0.6, respectively, within the typical range. Additionally, the momentum (viscosity) flux limiter is set to 0.5.

3. Results and discussions

3.1. Divertor/SOL plasma conditions in different scenarios

A comprehensive characterization of the target plasma density (n_e) and temperature (T_e) profiles across three simulated scenarios at a Ne puffing rate ($\Gamma_{Ne,puff}$) of 1.0×10^{20} s^{-1} is presented in figure 4. To analyze the target profiles in figure 4, two-dimensional distributions of deuterium ion (D^+)

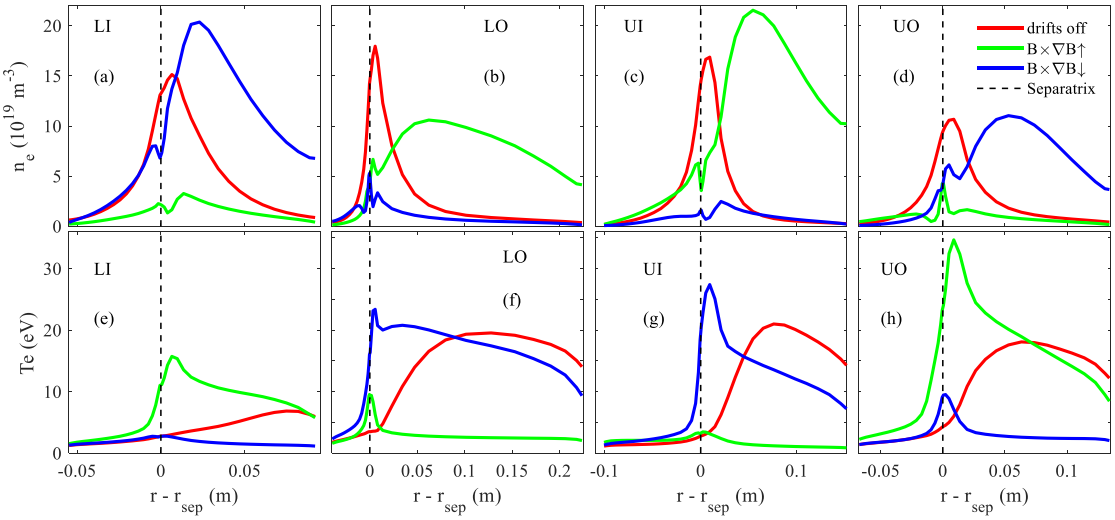

Figure 4. The target profiles of plasma density (n_e) ((*a*)–(*d*)) and temperature (T_e) ((*e*–(*h*)) for the simulation case with a Ne puffing rate of 1.0×10^{20} s^{-1} plotted versus distances to the strike-points. Three distinct scenarios are compared: (1) the absence of ion drifts (red), (2) full ion drifts with a downward $\boldsymbol{B}\times\nabla B$ direction ($\boldsymbol{B}\times\nabla B\downarrow$) (blue), and (3) full ion drifts with an upward $\boldsymbol{B}\times\nabla B$ direction ($\boldsymbol{B}\times\nabla B\uparrow$) (green).

fluxes within the B2.5 computational domain are illustrated in figures 5(*a*)–(*c*).

First, we examine the drift-free scenario illustrated in figure 5(*a*). In this scenario, the parallel flow of D^+ counteracts anomalous diffusion across magnetic field lines, balancing ionization and recombination sources and sinks. As a result, some plasma ions crossing the separatrix diffuse from the near SOL to the far SOL, while others are transported from the main SOL to the divertor targets. This transport replenishes plasma ions recycling to neutrals at the vessel walls and target plates. The poloidal velocity stagnation points of D^+ ions [1, 33, 52], which have been proved to be of paramount importance to the motion of impurity ions after originating from neutrals [33], are predominantly located at the mid-plane on both high-field and low-field sides. In the near SOL, strong thermal forces arising from temperature gradients (∇T) inhibit the downward transport of plasma ions from the hotter upstream SOL to the colder divertor region, significantly suppressing poloidal flow compared to the far SOL. Additionally, these strong thermal forces can induce a secondary stagnation point in the near divertor SOL, causing flow reversal [1]. Here, D^+ ions poloidally flow from the divertor region back to the main SOL. As a result, plasma ions recycling to neutrals at near SOL targets cannot be fully replenished by upstream ions but are partially offset by ions from the PFR. Plasma ions predominantly flow from the LO/UO to LI/UI divertor region via the PFR due to the relatively high ionization source of D^+ ($S_D{}^+$) in the LO/UO divertor region compared to the LI/UI one (figure 6). The radial D^+ flux in the near SOL significantly exceeds that in the far SOL across all four divertor regions, leading to very limited transport of main and impurity ions from the near SOL to the far SOL. This D^+ flow pattern leads to n_e peaks at the target plates within the common flux region (CFR) near the separatrix, while n_e values in the far SOL remain low. Notably, T_e values are higher in the far SOL than in the near SOL in this scenario.

In simulations incorporating both the $\boldsymbol{E}\times\boldsymbol{B}$ and diamagnetic drifts, the physics becomes more intricate. The parallel flow of D^+ ion balances the divergent part of ∇B and $\boldsymbol{E}\times\boldsymbol{B}$ drifts, compensating for anomalous diffusion across magnetic field lines and addressing ionization and recombination sources and sinks. Notably, the motion of plasma and impurity ions following their generation from neutrals is governed by the poloidal flux and its stagnation point, which fundamentally differ from the parallel dynamics. Therefore, the poloidal components of the ion flow shown in figures 5(*b*) and (*c*) arise from the vector sum of three contributions: (1) the poloidal projection of the parallel flow, (2) the poloidal components of the $\boldsymbol{E}\times\boldsymbol{B}$ and ∇B drifts, and (3) to a lesser extent, the component closing the anomalous diffusion term ($-D_\perp.\nabla$n).

In the upward ion $\boldsymbol{B}\times\nabla B$ drift scenario (figure 5(*b*)), D^+ ions predominantly exit the core plasma through the top portion of the separatrix near the upper X-point, with a minor fraction re-entering the core via the bottom portion. The combined effects of $\boldsymbol{E}\times\boldsymbol{B}$ drift and Pfirsch-Schlüter (PS) flows through the HFS SOL shift the poloidal velocity stagnation point of D^+ ions from the IMP toward the UI target plate, directing most of the D^+ flux from core into the LI divertor region. On the LFS, the same mechanisms alter the D^+ flow pattern between the OMP and the LO target plate, channeling the core D^+ flux toward the UO divertor region. The $\boldsymbol{E}\times\boldsymbol{B}$ drift through the PFR further redistributes ions from the LI/UO to LO/UI divertor region. These effects lead to a reduction or reversal of the radial D^+ flux in the near SOL of the LI and UO divertor regions, and a reversal of flux across the separatrix (from CFR to PFR). As a result, n_e is significantly reduced at the LI and UO target plates, leading to peaked T_e profiles due to the decreased n_e, near the separatrix. The radial $\boldsymbol{E}\times\boldsymbol{B}$ drift enhances the radial particle transport in the LO and UI divertor regions, promoting ion transport from the PFR to the CFR across the separatrix and from the near SOL to the far SOL, resulting in an outward shift of the n_e peak and an inward

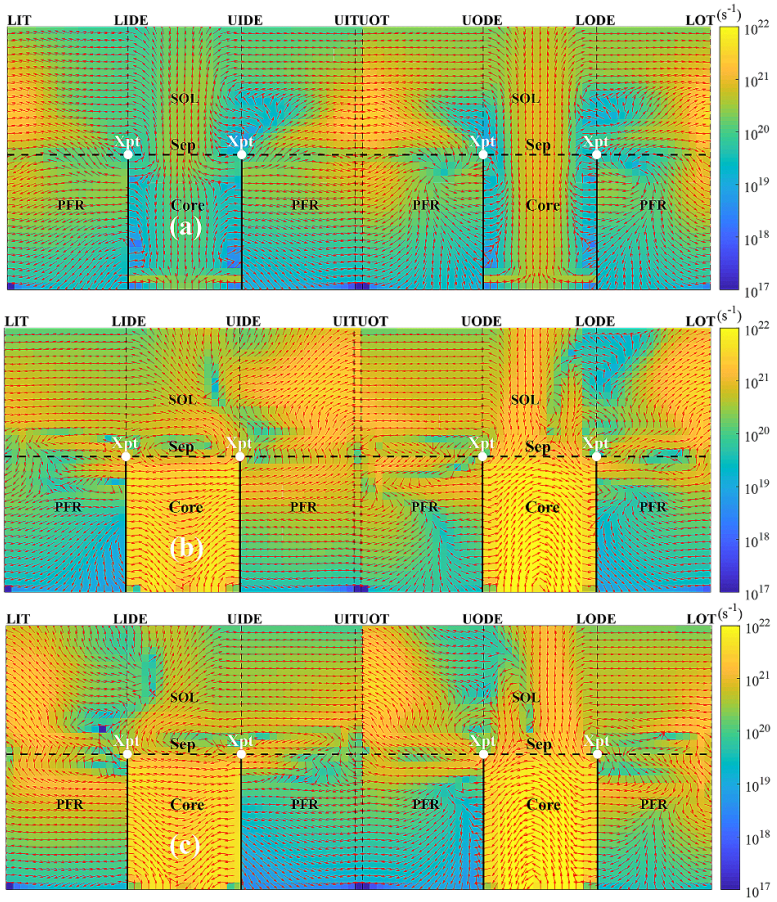

Figure 5. The two-dimensional distributions of D^+ ion flux within the B2.5 computational mesh is illustrated for the simulation case with a Ne puffing rate of 1.0×10^{20} s^{-1}. Three simulated conditions are compared: (*a*) absence of ion drift effects, (*b*) presence of full ion drifts with an upward $\boldsymbol{B}\times\nabla B$ direction ($\boldsymbol{B}\times\nabla B\uparrow$), and (*c*) presence of full ion drifts with a downward $\boldsymbol{B}\times\nabla B$ direction ($\boldsymbol{B}\times\nabla B\downarrow$). Vertical lines, from left to right, indicate the positions of the LI target plate (LIT), LI divertor entrance (LIDE), UI divertor entrance (UIDE), UI target plate (UIT), UO target plate (UOT), UO divertor entrance (UODE), LO divertor entrance (LODE), and the LO target plate (LOT).

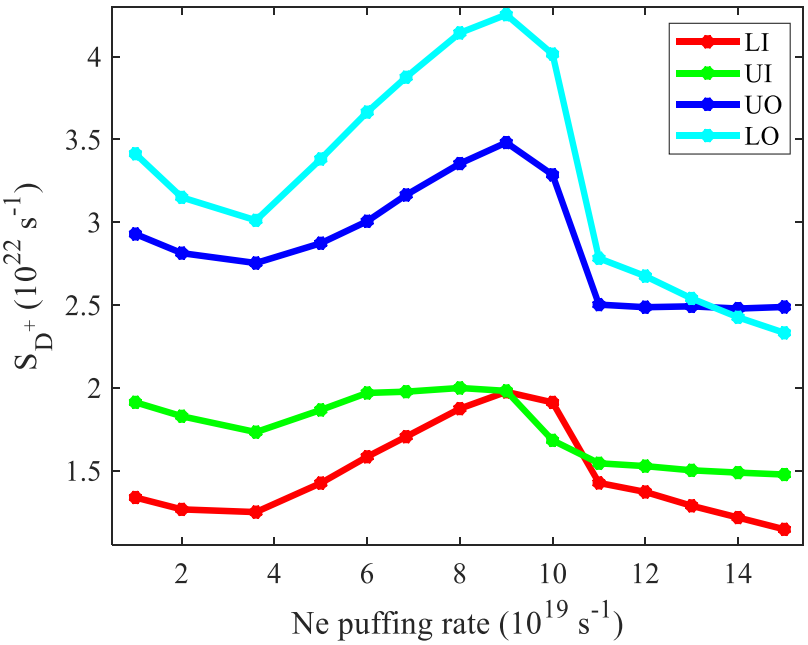

Figure 6. The D^+ ionization sources (S_{D^+}) in the four (LI, UI, UO, and LO) divertor regions under the drift-free scenario with varying neon puffing rates.

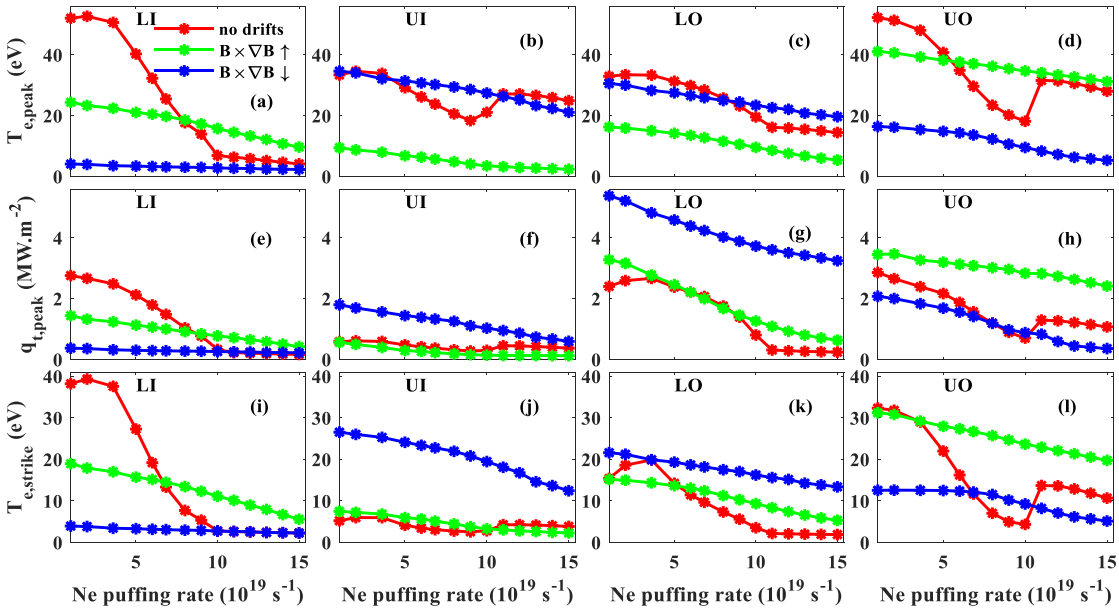

Figure 7. The peak (*a*)–(*d*) and strike-point (*i*)–(*l*) values of T_e and the peak values of divertor heat flux (*e*)–(*h*) at the LI, UI, LO and UO target plates plotted against $\Gamma_{\mathrm{Ne,puff}}$ for the three simulated scenarios.

shift of the T_e peak at the LO and UI target plates compared to the drift-free case. Additionally, flow reversal is observed in the CFR of the LO divertor region. In the core plasma region, a pronounced clockwise poloidal rotation is driven by strong radial electric fields.

In the downward ion $\boldsymbol{B}\times\nabla B$ drift scenario (figure 5(*c*)), the overall transport behavior is similar, but with reversed drift directions. D^+ ions predominantly exit the core through the bottom portion of the separatrix near the lower X-point, with a small fraction re-entering the core via the top portion. The $\boldsymbol{E}\times\boldsymbol{B}$ drift and PS flows in the HFS SOL shift the stagnation-point from the IMP toward the LI divertor target, directing D^+ ions from the core toward the UI divertor region. On the LFS, the flow pattern between the OMP and the UO divertor target is altered, with D^+ fluxes from core directed toward the UO divertor region. The $\boldsymbol{E}\times\boldsymbol{B}$ drift through the PFR transports D^+ ions from the LI/UO to LO/UI divertor region. Consequently, the radial D^+ flux in the near SOL is reduced or reversed in the LO and UI divertor regions, and the flux across the separatrix is reversed (from CFR to PFR) compared to the drift-free case. These changes result in a significant reduction in n_e at the LO and UI target plates, leading to peaked T_e profiles near the separatrix. The $\boldsymbol{E}\times\boldsymbol{B}$ drift enhances radial particle transport in the LI/UO divertor region, moving ions from the PFR to the CFR and from the near SOL to the far SOL, causing an outward shift of the n_e peak and an inward shift of the T_e peak at the LI/UO target plates. Moreover, the strong radial electric field in the outer core drives a strong counter-clockwise poloidal flow.

Compared to the drift-free state, the full-drift scenarios induce distinct modifications to the n_e profile. Specifically, the outward displacement of n_e peaks at the LO and UI (or LI and UO) targets for upward (or downward) ion $\boldsymbol{B}\times\nabla B$ drift is accompanied by a significant enhancement of n_e in the far SOL and a concurrent reduction in the PFR and near SOL. This behavior arises from the enhanced radial particle transport in the corresponding divertor region, driven by $\boldsymbol{E}\times\boldsymbol{B}$ drift, which facilitates ion migration from PFR to CFR and from the near SOL to the far SOL. Consequently, the reshaping of the target n_e profile induces corresponding modifications to the target T_e profile, resulting in a decrease of T_e in the far SOL and an increase of T_e in the near SOL and PFR (figure 4). To investigate the detailed impact of Ne impurity seeding levels on divertor plasma conditions across the three simulated scenarios, figure 7 depicts the peak ($T_{e,peak}$) and strike-point ($T_{e,strike}$) values of T_e and the peak divertor heat flux ($q_{t,peak}$) at the LI, LO, UI, and UO target plates as functions of the Ne puffing rate ($\Gamma_{\mathrm{Ne,puff}}$).

In no-drift scenarios, the radiative power losses (P_{rad}) in the divertor regions exhibit insensitivity to the increase in $\Gamma_{\mathrm{Ne,puff}}$ when the rate is below 4.0×10^{19} s^{-1} (figure 8). Consequently, $T_{e,peak}$, $T_{e,strike}$ and $q_{t,peak}$ exhibit minimal sensitivity to increases in $\Gamma_{\mathrm{Ne,puff}}$. Interestingly, these parameters may even increase slightly with rising $\Gamma_{\mathrm{Ne,puff}}$ due to reduced S_{D^+} (figure 6), which results in a decrease in plasma density in divertor regions. This behavior is sensitive to the reduced power flow from the upstream to divertor regions, caused by increased P_{rad} in the core and main SOL. As $\Gamma_{\mathrm{Ne,puff}}$ increases beyond 4.0×10^{19} s^{-1} up to 9.0×10^{19} s^{-1}, $T_{e,peak}$ and $T_{e,strike}$ as well as $q_{t,peak}$ decrease due to the significant increase in radiation power in the LI (from 0.059 MW to 0.118 MW), UI (from 0.093 MW to 0.141 MW), UO (from 0.146 MW to 0.267 MW) and LO (from 0.128 MW to 0.217 MW) divertor regions, the inner (from 0.024 MW to 0.107 MW) and outer (from 0.091 MW to 0.314 MW) SOL

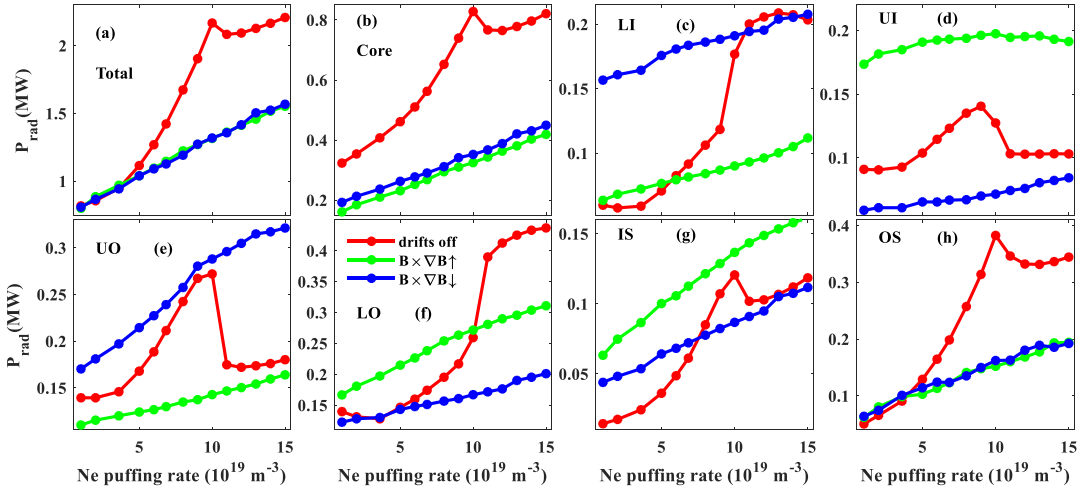

Figure 8. Total radiative power loss across the entire computational domain (*a*), including contributions from the core (*b*), the LI (*c*), UI (*d*), UO (*e*) and LO (*f*) divertor regions, as well as both the inner (*g*) and outer (*h*) SOL (IS/OS).

(IS/ OS) and the core (from 0.407 MW to 0.740 MW), as demonstrated in figure 8. Notably, with increasing $\Gamma_{\mathrm{Ne,puff}}$, the most pronounced reductions in $T_{\mathrm{e,peak}}$, $T_{\mathrm{e,strike}}$, and $q_{\mathrm{t,peak}}$ occur in the LI divertor, which is associated with its low and rapidly attenuating upstream power flow via the divertor entrance (P_{uDE}). Specially, P_{uDE} entering the LI divertor drops from 0.525 MW to 0.260 MW with Ne seeding. In contrast, the UI divertor exhibits a notably stable P_{uDE}, confined within 0.260–0.274 MW. The UO divertor receives the highest P_{uDE}, which experiences a significant but comparatively smaller reduction (1.096 MW to 0.712 MW). Conversely, the LO divertor maintains a relatively high P_{uDE} with only a modest decrease from 0.762 MW to 0.659 MW. However, when $\Gamma_{\mathrm{Ne,puff}}$ increases from 9.0×10^{19} s^{-1}–1.1×10^{20} s^{-1}, a more rapid increase in P_{rad} occurs in the LI (from 0.118 MW to 0.200 MW) and LO (from 0.217 MW to 0.390 MW) divertor regions, while a simultaneous sudden decrease in P_{rad} is observed in the UI (from 0.140 MW to 0.103 MW) and UO (from 0.267 MW to 0.175 MW) divertor regions. This leads to a sudden increase in $T_{\mathrm{e,peak}}$ and $T_{\mathrm{e,strike}}$ as well as $q_{\mathrm{t,peak}}$ at the UI and UO target plates. This phenomenon is attributed to the so-called 'density redistribution' [52] of Ne particle among the different plasma regions, which will be discussed in detail in the subsequent section. Subsequently, as $\Gamma_{\mathrm{Ne,puff}}$ increases further up to 1.5×10^{20} s^{-1}, $T_{\mathrm{e,peak}}$, $T_{\mathrm{e,strike}}$, and $q_{\mathrm{t,peak}}$ at all four target plates decrease gradually.

As illustrated in figure 1(*a*), the strike-point on the LI target plate is relatively high-positioned, while that on the LO target plate is located near the corner. This magnetic configuration results in significantly higher neutral closure in the LO divertor compared to the LI divertor. Under drift-free conditions at low $\Gamma_{\mathrm{Ne,puff}}$ ($\Gamma_{\mathrm{Ne,puff}} < 4.0 \times 10^{19}$ s^{-1}), the LI divertor (with $T_{\mathrm{e,peak}}/T_{\mathrm{e,strike}}$ varying from 52.04/38.20 eV to 50.61/37.57 eV) exhibits higher T_{e} target values than the LO divertor (with $T_{\mathrm{e,peak}}/T_{\mathrm{e,strike}}$ varying from 32.93/15.39 eV to 33.30/19.86 eV), despite receiving a lower upstream power flow ($P_{\mathrm{uDE,LI}}$) than the LO divertor ($P_{\mathrm{uDE,LO}}$), with $P_{\mathrm{uDE,LO}}/P_{\mathrm{uDE,LI}} \approx 1.25$–$1.6$. Nevertheless, the LI divertor demonstrates a stronger tendency for detachment ($T_{\mathrm{e}} < 5$ eV) compared to other divertors (LO, UI, and UO). This enhanced detachment is attributed to two factors: first, the low-magnitude P_{uDE} that undergoes pronounced attenuation (as previously noted) with increasing $\Gamma_{\mathrm{Ne,puff}}$; and second, the redistribution of Ne particle density toward the lower divertor. Additionally, the UO target plate ($T_{\mathrm{e,peak}}/T_{\mathrm{e,strike}}$ = 52.22/32.31 eV to 28.02/10.67 eV) maintains higher plasma temperatures than the UI target ($T_{\mathrm{e,peak}}/T_{\mathrm{e,strike}}$ = 33.38/5.21 eV to 24.91/3.84 eV) under drift-free conditions, consistent with substantially greater upstream power flow delivered to the UO divertor ($P_{\mathrm{uDE,UO}}$) compared to the UI one ($P_{\mathrm{uDE,UI}}$) ($P_{\mathrm{uDE,UO}}/P_{\mathrm{uDE,UI}} \approx 2.3$–$4.8$). When $\Gamma_{\mathrm{Ne,puff}}$ exceeds 1.0×10^{20} s^{-1}, both $T_{\mathrm{e,peak}}$ and $T_{\mathrm{e,strike}}$ at the LI target plate decrease below 5 eV, causing the LI divertor to enter the detached operation regime. At $\Gamma_{\mathrm{Ne,puff}} = 1.0 \times 10^{20}$ s^{-1}, the strike-point values of T_{e}, at the UI, UO and LO target plates, decrease below 5 eV; however, the peak values of T_{e} remain above 10 eV even when $\Gamma_{\mathrm{Ne,puff}}$ is increased to 1.5×10^{20} s^{-1}. Therefore, under drift-free conditions, only partial detachment near the strike-point occurs in the UI, UO, and LO divertors, even at high $\Gamma_{\mathrm{Ne,puff}}$ values. The redistribution of Ne density can even result in the reattachment of the UO divertor, with $T_{\mathrm{e,peak}}/T_{\mathrm{e,strike}}$ as high as 28.02/10.67 eV at $\Gamma_{\mathrm{Ne,puff}} = 1.5 \times 10^{20}$ s^{-1}.

The inclusion of drift effects in the simulations substantially modifies the divertor plasma conditions. In the full-drift scenario, where an upward ion $\boldsymbol{B}\times\nabla B$ drift is present, the $\boldsymbol{E} \times \boldsymbol{B}$ drift predominantly transports plasma and impurity ions from the LI/UO divertor region to the LO/UI one via the PFR, as shown in figures 2 and 5. Consequently, plasma in the LI/UO divertor region exhibits higher temperatures compared to the LO/UI divertor region. The in-out asymmetry in plasma parameters for the lower divertor (characterized by the ratio of $T_{\mathrm{e,peak}}$ at LI target plate to that at LO one, i.e. $T_{\mathrm{e,peak,LI}}/T_{\mathrm{e,peak,LO}}$, ranging from 1.47 to 1.81)

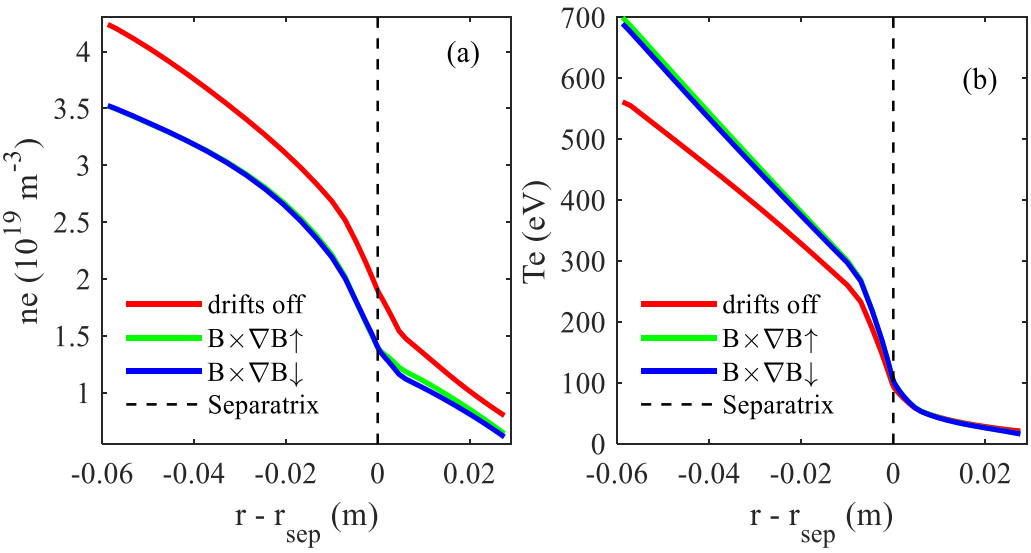

Figure 9. Radial profiles of n_e (*a*) and T_e (*b*) at the OMP for the simulation case at $\Gamma_{Ne,puff} = 1.0 \times 10^{20}$ s^{-1}. Three distinct scenarios are compared.

is less pronounced compared to that for the upper divertor (characterized by the ratio of $T_{e,peak}$ at UO target plate to that at the UI one, i.e. $T_{e,peak,UO}/T_{e,peak,UI}$, ranging from 4.35 to 13.14). As $\Gamma_{Ne,puff}$ increases, both the plasma temperature and divertor heat load progressively decrease due to enhanced radiative power loss across the entire computational domain. Furthermore, the UO divertor region exhibits a greater difficulty in achieving detachment ($T_e < 5$ eV), even at high Ne puffing rates, with $T_{e,peak}/T_{e,strike}$ as high as 31.22/19.74 eV at $\Gamma_{Ne,puff} = 1.5 \times 10^{20}$ s^{-1}.

The reversal of the ion $\boldsymbol{B}\times\nabla B$ drift direction leads to corresponding variations in the divertor plasma conditions. For downward ion $\boldsymbol{B}\times\nabla B$ drift, the $\boldsymbol{E} \times \boldsymbol{B}$ drift predominantly transports plasma and impurity ions from the LO/UI to LI/UO divertor region through the PFR (figures 2 and 5). Consequently, the plasma in the LO/UI divertor region becomes hotter compared to the LI/UO divertor region. The in-out asymmetry in plasma parameters becomes more pronounced for the lower divertor (characterized by the ratio of $T_{e,peak}$ at the LO target plate to that at the LI one, i.e. $T_{e,peak,LO}/T_{e,peak,LI}$, ranging from 7.49 to 8.56) than that for the upper divertor (characterized by the ratio of $T_{e,peak}$ at the UI target plate to that at the UO one, i.e. $T_{e,peak,UI}/T_{e,peak,UO}$, ranging from 2.11 to 3.98). The LI divertor region can achieve detachment ($T_e < 5$ eV) at extremely low $\Gamma_{Ne,puff}$ ($\Gamma_{Ne,puff} = 1.0\times 10^{19}$ s^{-1}) values, while the UO divertor detaches when $\Gamma_{Ne,puff}$ exceeds 1.0×10^{20} s^{-1}. However, both the LO and UI divertor regions remain difficult to detach even at high $\Gamma_{Ne,puff}$ values, with $T_{e,peak}/T_{e,strike}$ as high as 19.65/13.37 eV for LO target plate and $T_{e,peak}/T_{e,strike}$ reaching 21.08/12.43 eV for UI target plate at $\Gamma_{Ne,puff} = 1.5 \times 10^{20}$ s^{-1}. No significant redistribution of Ne impurity density is observed in both full drift scenarios. Furthermore, unlike previous studies on SN plasma configurations [53], in the present CDN plasma configuration, the in-out asymmetries in plasma parameters for both the upper and lower divertors tend to increase with $\Gamma_{Ne,puff}$, regardless of the drift flow directions. This behavior may be attributed to the combined contributions of $\boldsymbol{E} \times \boldsymbol{B}$ drift flows through both the PFR and SOL to the divertor asymmetry in CDN plasmas.

Furthermore, as illustrated in figure 8, the total radiative power loss (P_{rad}) in the entire computational domain exhibits negligible dependence on the drift direction. However, drifts significantly impact the contributions to P_{rad} from the four divertor regions and the inner SOL. Neglecting drift effects would lead to an overestimation of P_{rad} in both the entire domain and the core plasma region. This discrepancy is consistent with the markedly higher effective charge number (Z_{eff}) observed in drift-free simulations compared to full-drift scenarios. Specifically, across $\Gamma_{Ne,puff}$ levels, core-averaged Z_{eff} ranges from 1.48 to 3.05 without drifts, whereas with full drifts it varies from 1.19/1.24–1.71/1.79 for upward/-downward ion $\boldsymbol{B}\times\nabla B$ drift direction. Consequently, as shown in figure 9, eliminating drifts in simulations increases the upstream plasma density while decreasing its temperature relative to full-drift cases. Notably, the radial profiles of electron density (n_e) and temperature (T_e) at the outboard midplane remain largely invariant to drift direction. These phenomena are driven by drift-induced modulation of Ne impurity transport, which is analyzed in detail in section 3.2.

3.2. Neon impurity transport

Figure 10 presents the two-dimensional distributions of Ne impurity density across the entire computational domain for the three simulated scenarios at $\Gamma_{Ne,puff} = 1.0 \times 10^{20}$ s^{-1}. Without drift effects (figure 10(*a*)), Ne particles concentrate predominantly in the core plasma and main SOL, with a sharper density peak near the core boundary relative to the divertor regions. At this puffing rate, Ne density is higher in

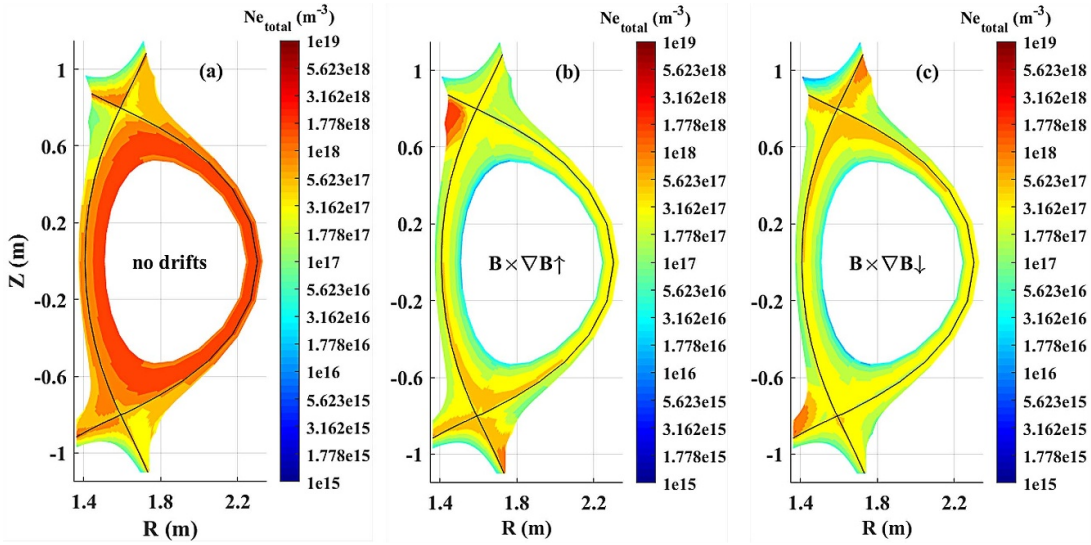

Figure 10. Two-dimensional distributions of Ne density for the three simulated scenarios at $\Gamma_{\mathrm{Ne,puff}} = 1.0 \times 10^{20}$ s^{-1}.

the LI and UO divertor regions compared to the LO and UI divertor regions. When drift effects are introduced, Ne density in both the core plasma and main SOL exhibits significant reductions. Under full-drift conditions, for upward ion $\boldsymbol{B}\times\nabla B$ drift, Ne density is higher in the LO/UI divertor region compared to the LI/UO divertor region. Conversely, for downward ion $\boldsymbol{B}\times\nabla B$ drift, Ne density is higher in the LI/UO divertor region compared to the LO/UI divertor region. Notably, in full-drift scenarios, Ne density near the lower (upper) X-point is higher compared to the upper (lower) X-point, during upward (downward) ion $\boldsymbol{B}\times\nabla B$ drift. Additionally, for the full-drift scenarios within the core plasma region, Ne density tend to concentrate near the separatrix rather than the core boundary.

Figure 11 illustrates the spatially averaged Ne density across various plasma regions as a function of $\Gamma_{\mathrm{Ne,puff}}$ for the three simulated scenarios. In no-drift scenarios, Ne density in all plasma regions increases proportionally with $\Gamma_{\mathrm{Ne,puff}}$ when $\Gamma_{\mathrm{Ne,puff}}$ is below 1.0×10^{20} s^{-1}. A critical transition occurs at $\Gamma_{\mathrm{Ne,puff}} = 1.0 \times 10^{20}$ s^{-1}, where Ne density in the LI divertor sharply escalates to over three times the density observed at lower puffing rates. Further increasing $\Gamma_{\mathrm{Ne,puff}}$ to 1.1×10^{20} s^{-1} results in a significant surge in Ne density within both the LI (doubling) and LO (increasing to ∼3.7 times) divertor regions. Concurrently, a substantial decrease in Ne density is observed in the UI (∼40% reduction) and UO (∼50% reduction) divertor regions, the inner (∼11% reduction) main SOL and core (∼10% reduction), with the growth rate of Ne density in core diminishing, indicative of a redistribution of Ne density among different plasma regions. Beyond $\Gamma_{\mathrm{Ne,puff}} = 1.1 \times 10^{20}$ s^{-1}, up to 1.5×10^{20} s^{-1}, Ne density increases gradually across all plasma regions with $\Gamma_{\mathrm{Ne,puff}}$. As shown in figure 10, the inclusion of drifts in simulations significantly impacts the Ne density across all divertor regions for the entire range of $\Gamma_{\mathrm{Ne,puff}}$. Specifically, the spatially averaged Ne density in the outer SOL, core, and entire computational domain decreases by more than 50% and 60% and 50%, respectively. The direction of ion $\boldsymbol{B}\times\nabla B$ drift notably affects Ne density in the LI, UI, UO, and LO divertor regions. However, the spatially averaged Ne density in upstream regions, including the inner and outer SOL and core, is minimally affected by drift direction. Furthermore, the spatially averaged Ne density across the entire computational domain remains nearly constant irrespective of drift direction. In both full-drift scenarios, no significant redistribution of Ne density is observed; instead, the Ne density in all plasma regions increases proportionally with $\Gamma_{\mathrm{Ne,puff}}$.

Generally, the particle density of a specific species in a plasma region is determined by particle sources, sinks, and flux divergence. In most plasma regions, the primary particle source stems from the ionization of neutral atoms, which originate from gas puff, volume recombination, or surface recycling at PFCs, particularly at target plates. Our simulations demonstrate that the recombination rate for Ne impurities ranges from 10^5 s^{-1}–10^{10} s^{-1}, with Ne seeding levels spanning 1.0×10^{19} s^{-1}–1.5×10^{20} s^{-1}. In contrast, under the assumption of full recycling, the recycling rate typically falls within 10^{20}–10^{22} s^{-1}, establishing it as the dominant contributor. From figure 12, the integrated ionization source (S_{Ne^+}) of Ne^+ from Ne atoms, which can be expressed as $S_{\mathrm{Ne}^+} = \int^{n_{\mathrm{Ne}^0}} n_e \overline{\sigma v_{iz}}(T_e)\,\mathrm{d}V$ (where n_{Ne^0} is the neutral Ne density and $\overline{\sigma v_{iz}}(T_e)$ is the ionization rate coefficient), varies between 9×10^{19} s^{-1} and 3×10^{21} s^{-1} across all simulation cases. Additionally, the LO/UO divertor region consistently exhibits higher total S_{Ne^+} compared to the LI/UI divertor region across all three simulated scenarios and the entire $\Gamma_{\mathrm{Ne,puff}}$ range, sustaining the Ne ion flux from the LO/UO to LI/UI divertor region through the PFR in the drift-free scenario. Furthermore, a strong S_{Ne^+} is observed in the upstream, including the main SOL and core, in drift-free scenarios. This observation can be attributed to two primary factors: the injection of neon gas from a specific segment at the OMP and the relatively high first ionization energy of neon atoms (21.56 eV), which influences

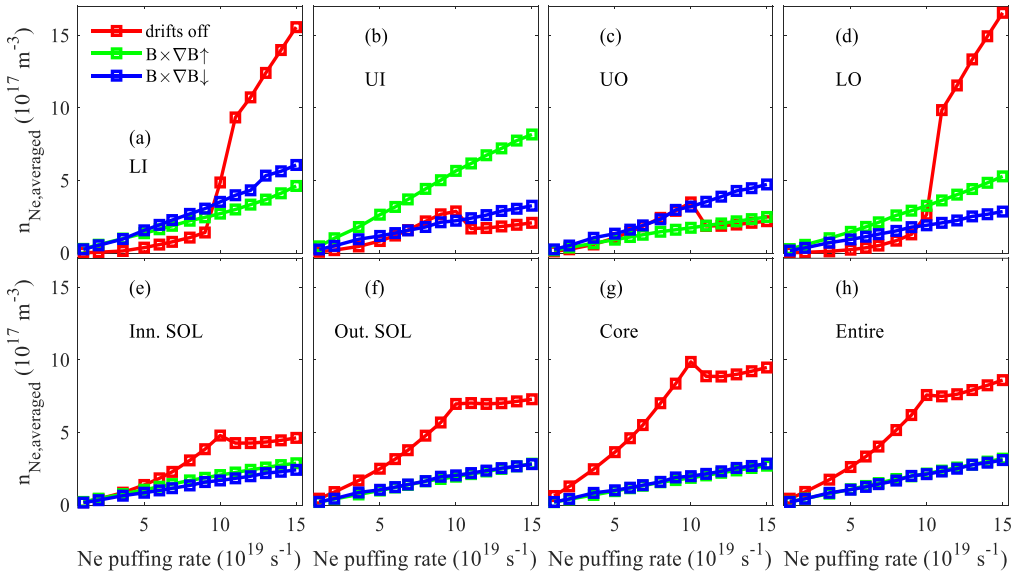

Figure 11. The spatially averaged Ne density in various plasma regions—LI, UI, UO and LO divertor regions, inner and outer SOL, core, as well as the entire computational domain—plotted against $\Gamma_{\mathrm{Ne,puff}}$ for the three simulated scenarios.

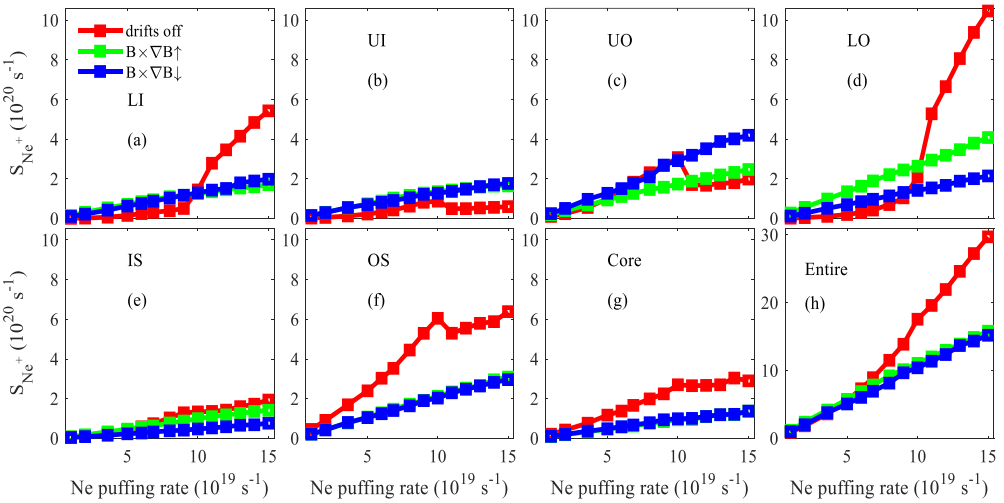

Figure 12. The integrated ionization source of Ne^+ (S_{Ne^+}) from Ne atoms for the three simulated scenarios at various plasmas regions plotted versus $\Gamma_{\mathrm{Ne,puff}}$.

its ionization behavior. The inclusion of drifts in the simulations significantly alters S_{Ne^+} in all plasma regions. However, S_{Ne^+} in the LI and UI divertors, outer SOL, core, and the entire computational domain shows insensitivity to the direction of ion $\boldsymbol{B}\times\nabla B$ drift. This explains why the spatially averaged Ne density over the entire computational domain remains nearly unchanged when the drift direction is reversed. Another critical process influencing the Ne density distribution is the particle transport, which will be discussed in the following.

According to previous findings [52], the neutral particle dynamics counteract impurity density redistribution by balancing the enhanced parallel impurity ion flux across plasma regions through the PFR and main SOL. The observed Ne density redistribution as $\Gamma_{\mathrm{Ne,puff}}$ increases in the drift-free scenario is predominantly governed by ion flows, sustained by the ionization source in different divertor regions, rather than neutral fluxes. Additionally, drift effects directly influence plasma ion transport. Hence, to elucidate the transport properties of Ne impurity ions in the divertor/SOL plasma regions, figure 13 presents the integrated ion fluxes at test surfaces labeled P1 to P6. The precise locations of these surfaces are indicated in figure 13(*g*), along with the definitions of the positive flux directions. As demonstrated in figure 13, both drift effects and $\Gamma_{\mathrm{Ne,puff}}$ significantly modulate the Ne ion fluxes into/out of the divertors via the PFR and main SOL.

From figure 13, for no-drift scenarios, the higher total S_{Ne^+} (figure 12) in the LO divertor region compared to the LI one drives Ne ions from the LO to LI divertor region through the PFR. Similarly, in the upper divertor, fluxes transport Ne ions from the UO to UI divertor region through the PFR. On the

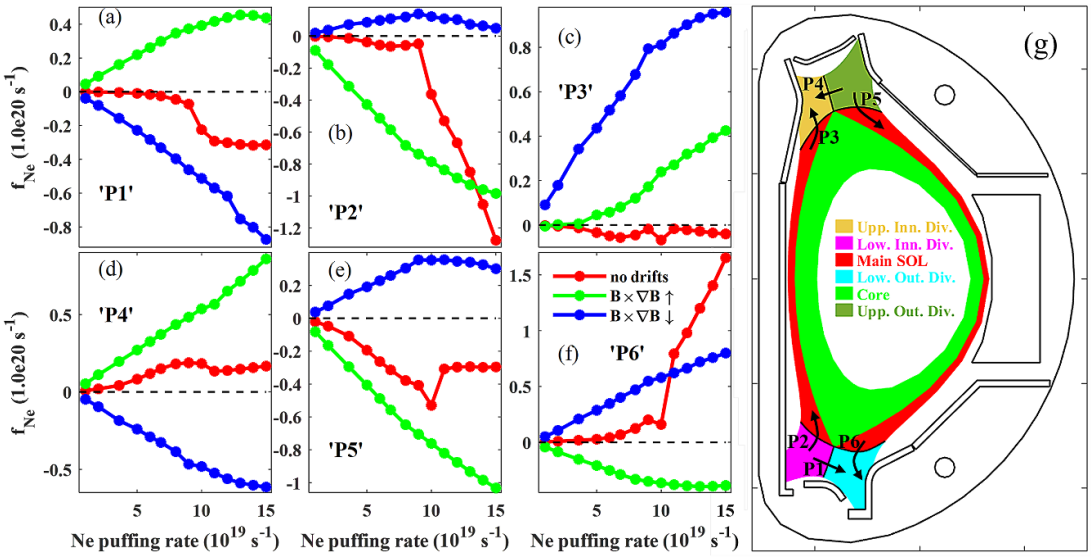

Figure 13. The integrated poloidal Ne ion flux transversing the test surfaces P1–P6 (*a*)–(*f*) is presented, with the positive directions of these fluxes indicated by arrows in panel (*g*).

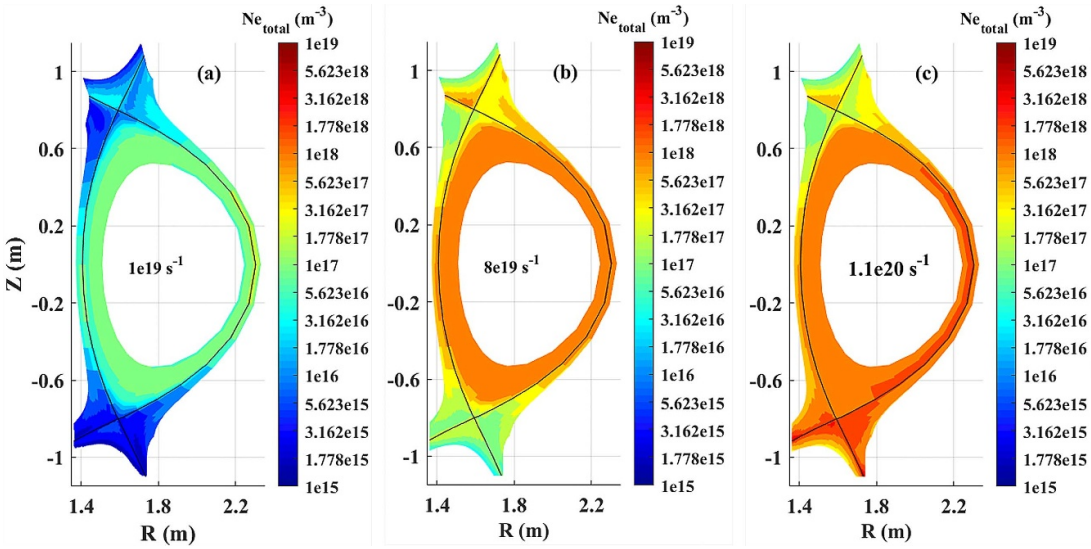

Figure 14. Two-dimensional distributions of Ne density in drift-free scenarios at different levels of $\Gamma_{\mathrm{Ne,puff}}$: (*a*) $\Gamma_{\mathrm{Ne,puff}} = 1.0 \times 10^{19}$ s^{-1}; (*b*) $\Gamma_{\mathrm{Ne,puff}} = 8.0 \times 10^{19}$ s^{-1}; (*c*) $\Gamma_{\mathrm{Ne,puff}} = 1.1 \times 10^{20}$ s^{-1}.

HFS, Ne ions are transported from the UI divertor region to the LI divertor region through the main SOL. Conversely, on the LFS, ions are transported from the main SOL to the UO and LO divertor regions via the divertor entrances. Notably, the direction of Ne ion fluxes through all test surfaces remains unaffected by the Ne puffing rate. When $\Gamma_{\mathrm{Ne,puff}}$ is below 1.0×10^{20} s^{-1}, the net influx of Ne ions into the UO divertor volume is significantly larger than into other divertor regions, explaining the observed higher Ne particle density in the UO divertor region (figure 14). Due to the relatively high Ne ion fluxes from the UO to UI divertor region through the PFR, Ne density in the PFR for the UI divertor region is larger than in the CFR under this condition. As $\Gamma_{\mathrm{Ne,puff}}$ increases to 1.0×10^{20} s^{-1}, the sharply increased Ne ion influx into the LI divertor region from the HFS SOL and from the LO divertor region (with the former dominating) leads to a significant increase in Ne density in the LI divertor region (figures 10(*a*) and 11). Further increasing $\Gamma_{\mathrm{Ne,puff}}$ to 1.1×10^{20} s^{-1} results in a sharp increase in Ne ion influx into the LO divertor region from the LFS SOL, while Ne ion influxes into the UO and UI divertor regions decrease. Consequently, Ne density in both the LI and LO divertor regions increases significantly, while Ne density in the UI and UO divertor regions decreases suddenly (figures 11 and 14). Finally, when $\Gamma_{\mathrm{Ne,puff}}$ is increased further beyond 1.1×10^{20} s^{-1} up to 1.5×10^{20} s^{-1}, Ne ion influx into the UI and UO divertor regions becomes insensitive to increases in $\Gamma_{\mathrm{Ne,puff}}$. As a result, Ne density in these regions increases slightly with $\Gamma_{\mathrm{Ne,puff}}$, while Ne ion influx into the LI

and LO divertor regions continues to rise at a high rate, leading to a remarkable increase in Ne density in these regions as $\Gamma_{\mathrm{Ne,puff}}$ increases (figure 11). It is notable that, although a large amount of Ne particles are transported into the LO divertor region at high levels of $\Gamma_{\mathrm{Ne,puff}}$ (beyond 1.0×10^{20} s^{-1}), the peak value of T_{e} at LO divertor target, which is typically located in the far SOL (figure 4) cannot be effectively decreased in the drift-free scenario (figure 7).

The inclusion of drifts in simulations significantly redistributes the Ne density among different divertor regions by modulating particle fluxes through the PFR and main SOL, as shown in figure 13. For upward ion $\boldsymbol{B}\times\nabla B$ drift, the $\boldsymbol{E}\times\boldsymbol{B}$ drift governs the transport of Ne ion fluxes from the LI to LO divertor region via the PFR. Simultaneously, in the upper divertor, the $\boldsymbol{E}\times\boldsymbol{B}$ drift drives Ne ions from the UO to UI divertor region through the PFR, consistent with the typical drift flow pattern illustrated in figure 2. On the HFS, Ne ions are transported from the main SOL to the LI and UI divertor regions through the divertor entrances. Conversely, on the LFS, ions are transported from the LO to UO divertor region through the main SOL. Notably, the direction of Ne ion fluxes through all test surfaces (P1 to P6) remains independent of the Ne seeding level, like that in drift-free scenarios. Furthermore, the net Ne ion influx into the UI divertor region is consistently larger than that into other divertor regions (LI, LO, UO), which explains the observed higher Ne particle density concentration in the UI divertor region, as shown in figure 10(*b*).

Notably, as $\Gamma_{\mathrm{Ne,puff}}$ increases, no abrupt variations are observed in the Ne ion fluxes crossing test surfaces under full-drift conditions. When the ion $\boldsymbol{B}\times\nabla B$ drift reverses direction (i.e. becomes downward), the Ne ion flux direction across all test surfaces (excluding P3) also reverses. In this scenario, the $\boldsymbol{E}\times\boldsymbol{B}$ drift governs the transport of Ne ion fluxes from the LO to LI divertor region through the PFR. Concurrently, in the upper divertor, the $\boldsymbol{E}\times\boldsymbol{B}$ drift drives Ne ions from the UI to UO divertor region through the PFR, consistent with the typical drift flow pattern depicted in figure 2. Additionally, on the HFS, Ne ions are transported from the LI to UI divertor region through the main SOL. In contrast, on the LFS, Ne ions are transported from the UO to the LO divertor region through the main SOL. Although the Ne ion flux from the HFS SOL to the UI divertor region via test surface P3 increases significantly, a substantial number of Ne ions are also transported from the UI to UO divertor region through the PFR via test surface P4. Hence, as the ion $\boldsymbol{B}\times\nabla B$ drift changes direction from upward to downward, the Ne density in the UI divertor region decreases markedly, as shown in figure 10. The detailed influences of the drift direction on the Ne ion flux pattern in the computational region will be further analyzed.

Figure 15 illustrates the typical Ne ion flux patterns within the computational domain for three simulated scenarios with a neon puffing rate of $\Gamma_{\mathrm{Ne,puff}} = 1.0 \times 10^{20}$ s^{-1}. Firstly, the drift-free scenario, shown in figure 15(*a*), is examined in detail. A strong $S_{\mathrm{Ne}}{}^{+}$ in core plasma region near the separatrix (figure 16) drives a substantial Ne ion flux from core to SOL via the separatrix and from the near SOL to the far SOL. In the far SOL, a portion of Ne ions are directed from the main SOL to the divertor regions through the divertor entrances, while the remainder are transported toward the main vessel. Within the near SOL, stagnation points for the poloidal velocity of Ne ions in divertor regions influences ion movement. Ne ions that undergo initial ionization from neutral atoms above these stagnation points exhibit migration behavior characterized by movement from the divertor regions to the main SOL, as previously documented [33]. Furthermore, in the core plasma region, a substantial fraction of Ne ions are transported deeper into the core boundary while being expelled away from the separatrix. This observation aligns with the measured Ne density distribution in the core, where higher Ne densities are observed near the core boundary compared to regions near the separatrix, as evidenced in figures 10 and 14.

Incorporating drift effects significantly reduces the concentration of $S_{\mathrm{Ne}}{}^{+}$ (figure 16) in core, thereby decreasing the Ne ion flux across the separatrix into the main SOL compared to drift-free scenarios (figure 15). A distinct rotational pattern of Ne ions is observed in the outer core near the separatrix. Additionally, the radial component of Ne ion flux is notably smaller in the core plasma region where $S_{\mathrm{Ne}}{}^{+}$ is more concentrated. Consequently, Ne ions undergoing their first ionization from neutral atoms near the separatrix are largely unable to penetrate deeper into the core. In full-drift scenarios, Ne density near the core boundary is approximately an order of magnitude lower than near the separatrix (figure 10). For upward ion $\boldsymbol{B}\times\nabla B$ drift, on the HFS, Ne ions are predominantly transported from the main SOL to LI divertor region, while on the LFS, Ne ions are driven from the main SOL to UO divertor region. Conversely, for downward ion $\boldsymbol{B}\times\nabla B$ drift, on the HFS, Ne ions are primarily transported from the main SOL to UI divertor region, while on the LFS, Ne ions are driven from the main SOL to LO divertor region. In the remaining two divertor regions (LO and UI for upward ion $\boldsymbol{B}\times\nabla B$ drift; LI and UO for downward ion $\boldsymbol{B}\times\nabla B$ drift), stagnation points for the poloidal velocity of Ne lead to divertor leakage of Ne ions that underwent their first ionization from neutral atoms above these stagnation points. However, Ne density in the divertor region (figure 10) seems to be predominantly determined by Ne ion flux through the PFR rather than that through the SOL. Transport of Ne ions from LI/UO to LO/UI divertor region through the PFR results in higher Ne density in the LO/UI divertor region compared to the LI/UO one for upward ion $\boldsymbol{B}\times\nabla B$ drift. Additionally, significant radial transport of Ne ions from the PFR to the CFR leads to more concentrated Ne density in the CFR of the UI divertor region (figure 10). Similarly, for downward ion $\boldsymbol{B}\times\nabla B$ drift, Ne density in the LI/UO divertor region tends to be larger than that in the LO/UI divertor region, with Ne density in the CFR being much higher than in the PFR for both the LI and UO divertor regions. The significant difference in the core contribution of $S_{\mathrm{Ne}}{}^{+}$ between drift-free scenarios and full-drift scenarios primarily results from variations in Ne ion radial transport in the main SOL (figure 15). In no-drift scenarios, a substantial number of Ne ions from core and divertor regions are transported through the main SOL to the vessel walls and subsequently recycled back as neutrals. These recycling neutrals can directly enter

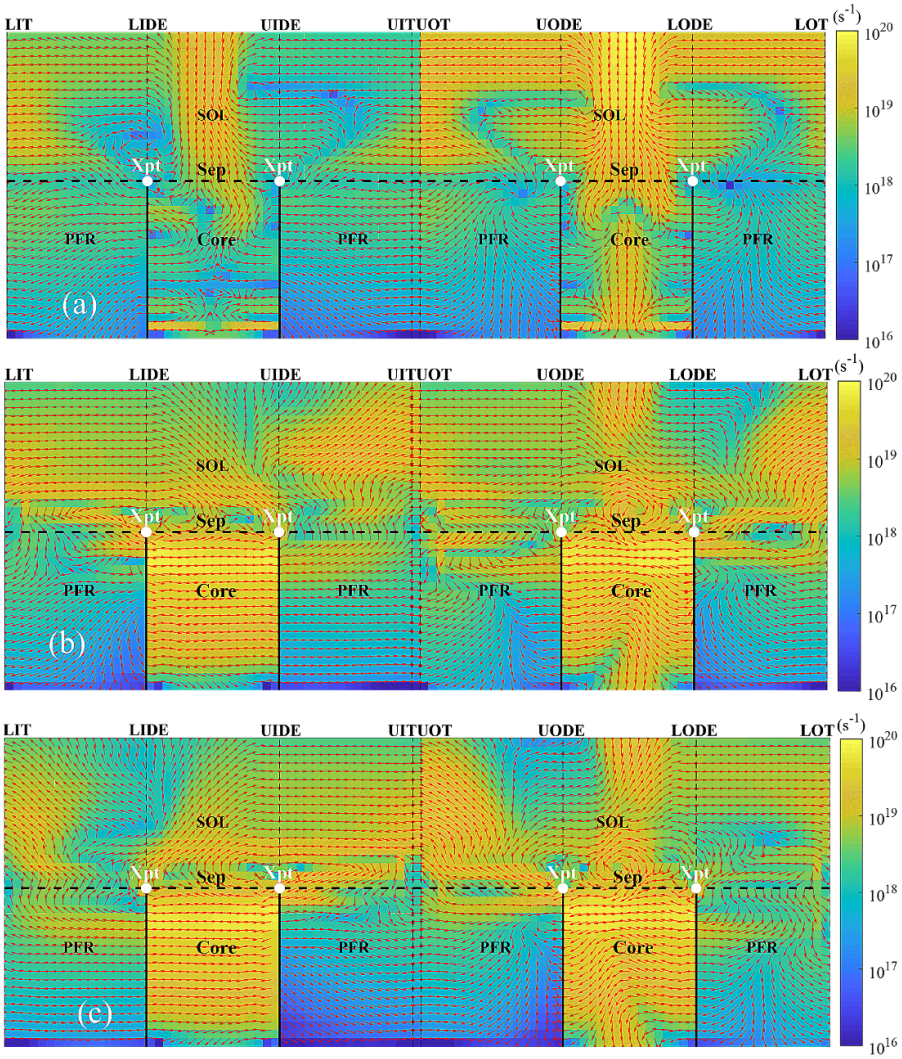

Figure 15. The two-dimensional distribution of Ne ion flux (summed over all the charge states) within the B2.5 computational mesh framework is illustrated for three simulated scenarios at a Ne puffing rate of $\Gamma_{\mathrm{Ne,puff}} = 1.0 \times 10^{20}$ s^{-1}: (*a*) absence of ion drift effects, (*b*) presence of full ion drifts with an upward $\boldsymbol{B}\times\nabla B$ direction ($\boldsymbol{B}\times\nabla B\uparrow$), and (*c*) presence of full ion drifts with a downward $\boldsymbol{B}\times\nabla B$ direction ($\boldsymbol{B}\times\nabla B\downarrow$). Vertical lines, from left to right, indicate the positions of the LI target plate (LIT), LI divertor entrance (LIDE), UI divertor entrance (UIDE), UI target plate (UIT), UO target plate (UOT), UO divertor entrance (UODE), LO divertor entrance (LODE), and the LO target plate (LOT).

the core, unconstrained by magnetic field lines, thereby sustaining the strong $S_{\mathrm{Ne}}{}^{+}$ in core. In contrast, in full-drift scenarios, the reduced level of Ne ion radial transport from main SOL to vessel walls leads to a decrease in the number of recycling Ne atoms and, consequently, a reduction in $S_{\mathrm{Ne}}{}^{+}$ in core.

According to [33], in full-drift scenarios, the poloidal velocity of Ne ions, which largely determines Ne divertor retention, can be estimated as the vector sum of the poloidal projection of the parallel velocity for Ne ($u_{\parallel,Ne}$) and the poloidal $\boldsymbol{E}\times\boldsymbol{B}$ drift velocity. Here, the former, i.e. $u_{\parallel,Ne}$, can be deduced from the parallel impurity force balance equation, the solution of which might be approximated as the balance of friction and thermal forces (i.e. $F_{\mathrm{th}} \approx -F_{\mathrm{fr}}$), while the other terms (e.g. the pressure gradient and electrostatic forces) are negligibly important. Generally, the main ion (D^{+}) flow determines the baseline of impurity flow. A deviation of the impurity flow from the main ion flow mainly due to the thermal force ($F_{\mathrm{th}} \propto Z^2\nabla T$). According to [52, 54], the difference between $u_{\parallel,\mathrm{Ne}}$ and the parallel velocity for D^{+} ($u_{\parallel,\mathrm{D}}$) is given by:

$$u_{\parallel,\mathrm{D}} - u_{\parallel,\mathrm{Ne}} = \frac{F_{\mathrm{fr}}}{c_{\mathrm{fr}}} \approx -\frac{F_{\mathrm{th}}}{c_{\mathrm{fr}}}. \tag{1}$$

Here, c_{fr} is the friction coefficient, $c_{\mathrm{fr}} \propto n_{\mathrm{D}}/T^{3/2}$ (n_{D} is the main ion (deuterium) density). Hence, the ratio of thermal force and friction coefficient compensates the background plasma flow at the position of stagnation-point for $u_{\parallel,\mathrm{Ne}}$ (i.e. $u_{\parallel,\mathrm{Ne}} = 0$):

$$u_{\parallel,\mathrm{D}} = \frac{F_{\mathrm{fr}}}{c_{\mathrm{fr}}}. \tag{2}$$

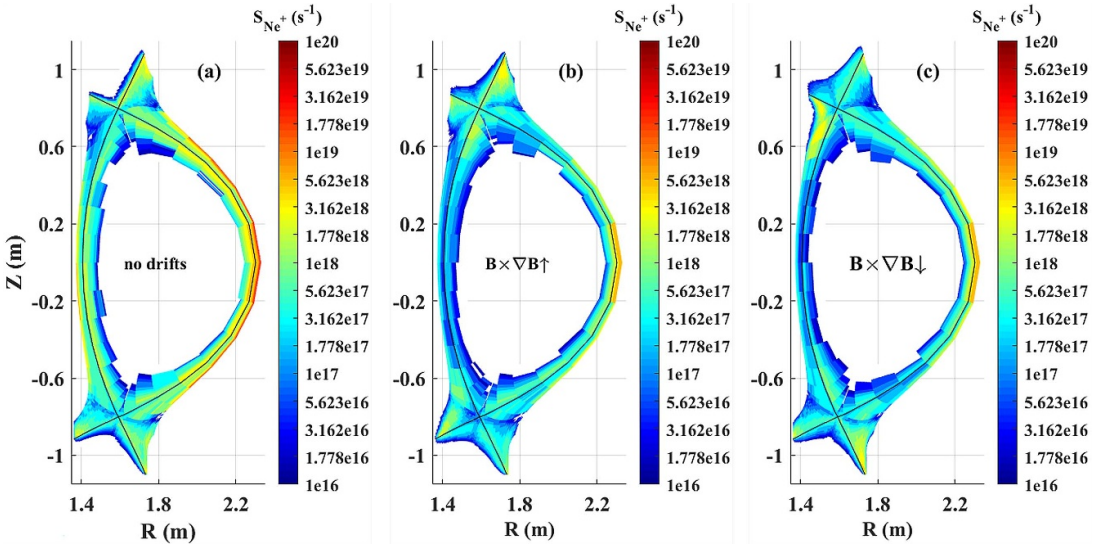

Figure 16. Two-dimensional distribution of Ne^+ ionization source from the neutral Ne atoms ($S_{Ne}{}^+$, in s^{-1}) for the three simulated scenario at a Ne puffing rate of $\Gamma_{\mathrm{Ne,puff}} = 1.0 \times 10^{20}$ s^{-1}.

Basically, F_{th} shifts the position of stagnation point for $u_{\parallel,\mathrm{Ne}}$ towards the divertor plate and thus tends to decrease the divertor retention of impurity ions. With $F_{\mathrm{th}} \propto \nabla T$, one obtains:

$$\frac{F_{\mathrm{th}}}{c_{\mathrm{fr}}} \propto \frac{T^{3/2}\nabla T}{n_{\mathrm{D}}}. \tag{3}$$

From equation (3), the decrease of temperature, induced by neon seeding, reduce the effect of thermal force due to the reduction of $\frac{F_{\mathrm{th}}}{c_{\mathrm{fr}}}$, moving the stagnation point for impurity towards that for main ion and further away from the target. Hence, from this point of view, impurity seeding has the potential to enhance divertor impurity retention at higher seeding levels. Nevertheless, in fact, this mechanism competes with the reduced divertor retention caused by the shifted neutral ionization front position [33, 52, 53]. A comparison of figures 5 and 15 reveals that in the far SOL, despite significant differences in magnitude, the Ne ion flux pattern's departure from D^+ flux pattern is nearly imperceptible in terms of the stagnation-point location for poloidal velocity. In contrast, in the near SOL, the stagnation point for the poloidal velocity of Ne ions ($u_{\mathrm{pol,Ne}}$)is positioned closer to the target compared to that for the poloidal velocity of D^+ ($u_{\mathrm{pol,D}}$). Consequently, based on the theoretical framework, it can be inferred that the value of $\frac{F_{\mathrm{fr}}}{c_{\mathrm{fr}}}$ in the far SOL is significantly smaller than in the near SOL, primarily due to the relatively lower temperature and temperature gradient in the far SOL compared to the near SOL.

The effects of $\Gamma_{\mathrm{Ne,puff}}$ on the stagnation point of the poloidal velocity for Ne ions ($u_{\mathrm{pol,Ne}}$) are illustrated in figure 17. In the drift-free scenario depicted in figures 17(*a*) and (*b*), $u_{\mathrm{pol,Ne}}$ exhibits no stagnation points in the far SOL of divertor regions. Consequently, Ne ions are transported from the upstream to divertor regions, as evidenced in figure 15(*a*). In the near SOL, for $\Gamma_{\mathrm{Ne,puff}}$ below 1.0×10^{20} s^{-1}, the stagnation point of $u_{\mathrm{pol,Ne}}$ is situated in the divertor region. This allows a significant number of Ne ions undergoing their first ionization in the LI divertor region to escape upstream through the near SOL. As a result, Ne density in the LI divertor region is relatively low, as shown in figure 14. The stagnation point for $u_{\mathrm{pol,Ne}}$ in the colder LI/LO divertor region shifts with increasing $\Gamma_{\mathrm{Ne,puff}}$, whereas the stagnation point in the hotter UI/UO region remains nearly unaffected by the seeding level (equations (1)–(3)). Furthermore, Ne-induced changes in temperature and density modulate the deuterium ionization source ($S_{\mathrm{D}}{}^+$), which governs the background flow structure in the main SOL. A qualitative restructuring of the main ion flow through the SOL occurs when $\Gamma_{\mathrm{Ne,puff}}$ reaches 1.0×10^{20} s^{-1}, a condition under which $S_{\mathrm{D}}{}^+$ in the LI divertor region surpasses that in the UI divertor region (figure 6). Consequently, the Ne stagnation points at the IMP and in the LI divertor are eliminated (figure 17), and the far SOL stagnation point shifts from the LI divertor region towards the UI divertor. This flow reorganization is characterized by a sharp increase in the main ion flow into the colder LI divertor and a concurrent decrease in the flow to the hotter UI divertor (figure 18). Consequently, at relatively high seeding levels ($\Gamma_{\mathrm{Ne,puff}} \geqslant 1.0 \times 10^{20}$ s^{-1}), a large portion of Ne ions is transported from the main SOL and UI divertor region into the LI divertor region, resulting in a sharp increase in Ne density in the LI divertor region (figures 10, 11, and 14). Similarly, when $\Gamma_{\mathrm{Ne,puff}}$ is increased to 1.1×10^{20} s^{-1}, $S_{\mathrm{D}}{}^+$ in the LO divertor region becomes comparable to that in the UO divertor region (figure 6). Consequently, the main ion flows into the LO and UO divertors are inverted (figure 18), triggering a qualitative change in the LFS SOL flow pattern and the disappearance of the $u_{\mathrm{pol,Ne}}$ stagnation points at the OMP and in the LO divertor. Consequently, a substantial number of Ne ions are transported from the main SOL and UO divertor region into the LO

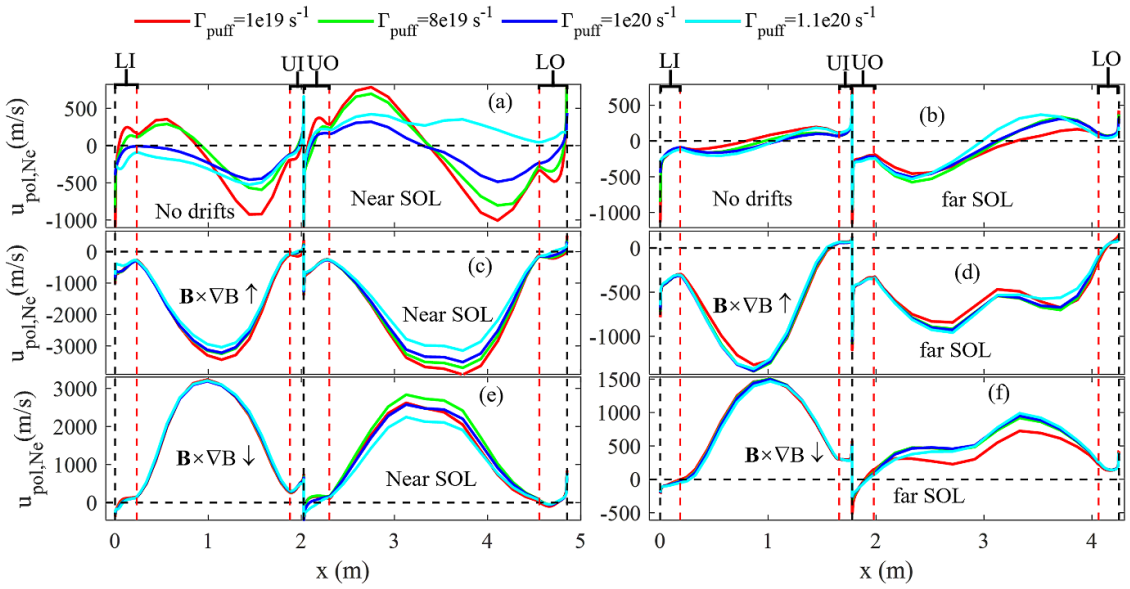

Figure 17. The poloidal profile of Ne poloidal velocity ($\bar{u}_{\mathrm{pol,imp}} = \Gamma_{\mathrm{pol,imp}}/n_{\mathrm{imp}}{}^{\mathrm{total}}$) at different levels of Ne puffing rate in the near and far SOL for the three simulated scenarios. Where, x is the poloidal distance from the LI divertor target plate, increasing in the clockwise direction. Positive vertical coordinates correspond to a clockwise poloidal velocity of Ne ions from the LI to the LO target plate. Black brackets in panels (*a*) and (*b*) indicate the locations of the LI, UI, UO, and LO divertor regions. Black dashed lines indicate the target plate locations, while red dashed lines mark the divertor entrance positions.

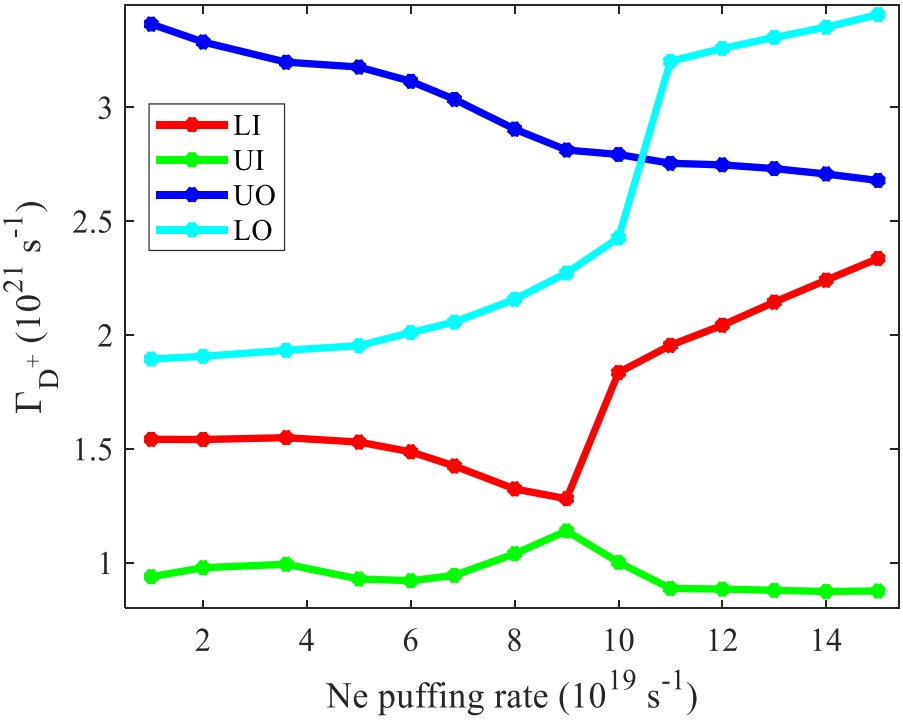

Figure 18. Integrated upstream D^+ flow (f_{D^+}) entering the divertors as a function of the Ne puffing rate.

divertor region through the LFS SOL, causing a significant rise in Ne density in the LO divertor region (figures 11 and 14).

The inclusion of drift effects in simulations significantly alters $u_{\mathrm{pol,Ne}}$. In full-drift scenarios, $u_{\mathrm{pol,Ne}}$ can be approximated as the vector sum of the poloidal projection of $u_{\parallel,Ne}$ and the poloidal $\boldsymbol{E} \times \boldsymbol{B}$ drift velocity [33]. As previously demonstrated [53], the structure and position of $u_{\mathrm{pol,Ne}}$ stagnation points are largely governed by the $\boldsymbol{E} \times \boldsymbol{B}$ drift pattern (figure 17). This pattern proves to be remarkably insensitive to increases in $\Gamma_{\mathrm{Ne,puff}}$. Therefore, even as $\Gamma_{\mathrm{Ne,puff}}$ rises, the fundamental flow structure that would facilitate a large-scale redistribution of Ne between the upper and lower divertors has

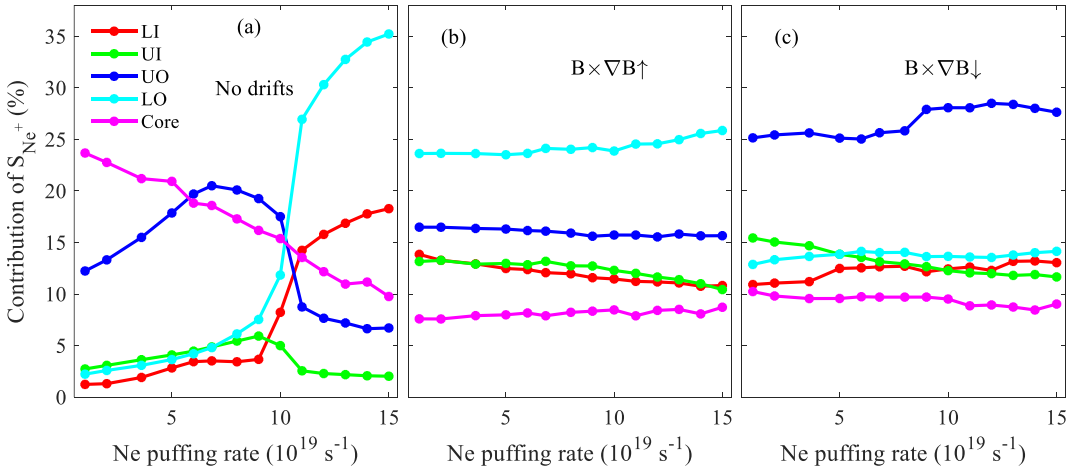

Figure 19. The relative percentage contribution of S_{Ne}^{+} from the LI, LO, UI, and UO divertors and core plotted against Ne puffing rate for three simulation scenarios.

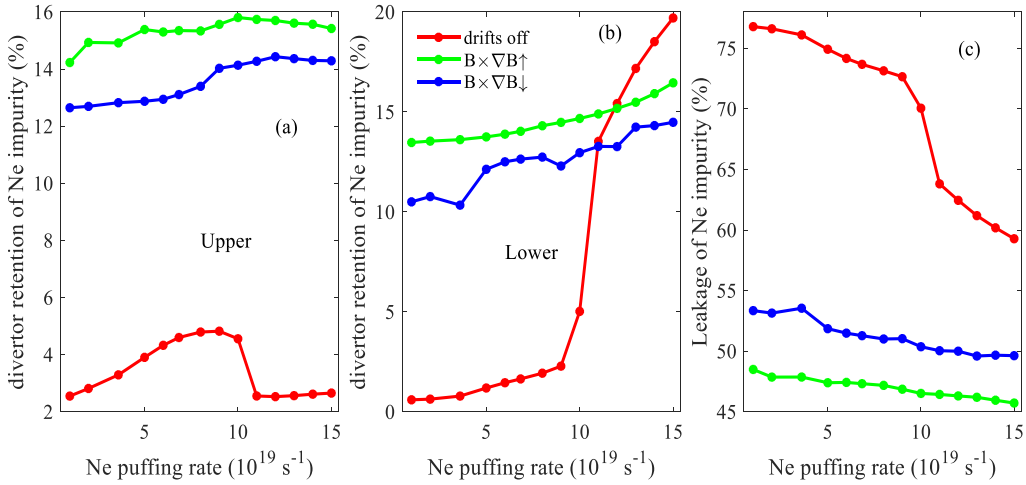

Figure 20. Ne impurity retention in the upper (*a*) and lower (*b*) divertors and core leakage plotted as a function of Ne puffing rate for three simulation scenarios.

not been observed in the full-drift scenarios. For upward ion $\boldsymbol{B}\times\nabla B$ drift, the poloidal $\boldsymbol{E}\times\boldsymbol{B}$ drift flow transports Ne ions from the UI divertor region to the LI divertor region through the SOL (figure 2). Consequently, no stagnation points for $u_{\mathrm{pol,Ne}}$ are observed in most of the LI divertor region, except in a narrow region near the separatrix. Similarly, no stagnation points for $u_{\mathrm{pol,Ne}}$ are present in most of the UO divertor region. As $\Gamma_{\mathrm{Ne,puff}}$ increases, the stagnation points for $u_{\mathrm{pol,Ne}}$ shift upstream. However, the influence of the seeding level on the position of these stagnation points is less pronounced compared to drift-free scenarios. The reversal of ion $\boldsymbol{B}\times\nabla B$ direction, does not significantly alter the fundamental physics but results in a poloidal displacement of the stagnation points for $u_{\mathrm{pol,Ne}}$.

Figure 19 shows the relative contribution of $S_{\mathrm{Ne}}{}^{+}$ from the divertor regions and core plasma to elucidate the influence of $\Gamma_{\mathrm{Ne,puff}}$ on its spatial distribution. An increase (decrease) in the divertor contribution indicates $S_{\mathrm{Ne}}{}^{+}$ migration toward (away from) the target plates. In drift-free scenarios, increasing $\Gamma_{\mathrm{Ne,puff}}$ causes the relative $S_{\mathrm{Ne}}{}^{+}$ contribution from the upper divertor (UI + UO) to first rise then decline, while the lower divertor (LI + LO) contribution increases progressively. This shift results from redistribution of Ne impurities toward the lower divertor, significantly enhancing the lower divertor's $S_{\mathrm{Ne}}{}^{+}$ contribution. Correspondingly, the neon divertor retention, defined as the ratio of neon particles retained in the divertor region to the total neon inventory in the computational domain, demonstrates divergent trends. In the upper divertor, Ne retention initially increases but subsequently decreases with rising $\Gamma_{\mathrm{Ne,puff}}$, whereas the lower divertor exhibits a monotonic increase (figures 20(*a*) and (*b*)). This aligns with ionization-front and stagnation-point mechanisms in SN plasmas [33]. Additionally, Ne leakage into the core, quantified as the ratio of neon particles in core to the total inventory within the computational domain, decreases substantially with $\Gamma_{\mathrm{Ne,puff}}$ (figure 20(*c*)), attributed to reduced

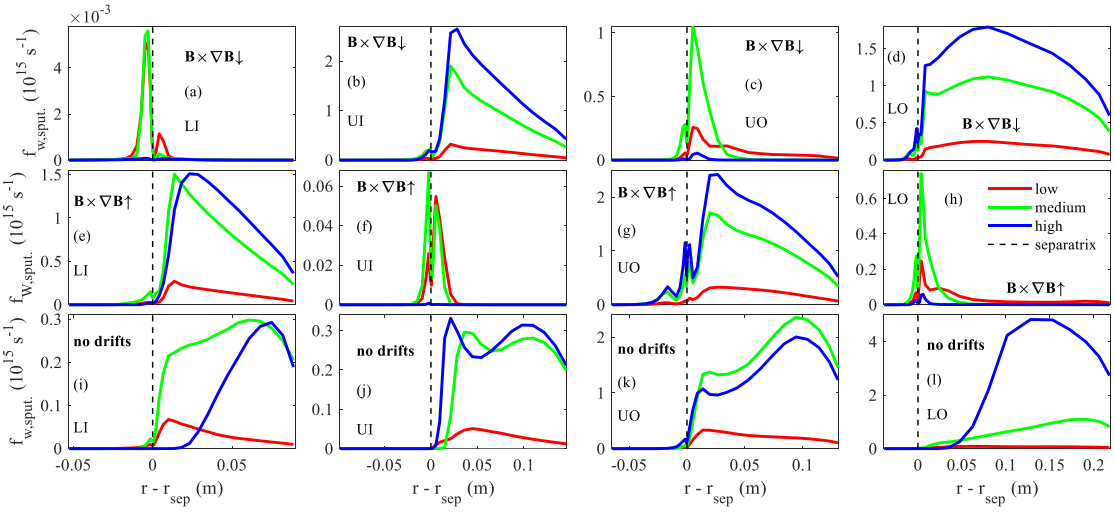

Figure 21. Profiles of W impurity sputtering flux (in s^{-1}) plotted against distance to strike point at the LI, UI, UO and LO target plates under low (1.0×10^{19} s^{-1}), medium (8.0×10^{19} s^{-1}), and high (1.5×10^{20} s^{-1}) levels of $\Gamma_{\mathrm{Ne,puff}}$ for the three simulated scenarios.

core $S_{\mathrm{Ne}}{}^{+}$ contribution and enhanced 'brushing' of Ne ions from upstream to the divertors through the main SOL. In contrast, under drift effects, $S_{\mathrm{Ne}}{}^{+}$ distribution becomes largely invariant to $\Gamma_{\mathrm{Ne,puff}}$. Consequently, at elevated $\Gamma_{\mathrm{Ne,puff}}$, full-drift simulations of CDN plasmas exhibit a moderately smaller increase in divertor Ne retention and a less significant reduction in Ne core leakage compared to SN configurations [53]. This behavior arises from the insensitivity of both $S_{\mathrm{Ne}}{}^{+}$ distribution and $u_{\mathrm{pol,Ne}}$ to $\Gamma_{\mathrm{Ne,puff}}$. Furthermore, compared to downward ion $\boldsymbol{B}\times\nabla B$ drift, upward ion $\boldsymbol{B}\times\nabla B$ drift results in higher divertor retention and lower core leakage.

3.3. *Effects of Ne seeding on W impurity behaviors*

The impact of externally introduced impurities on tungsten (W) impurity generation and transport is crucial for the high-power operation of EAST and future tokamaks, such as ITER. This study investigates how Ne impurity seeding affects the sputtering of W impurities from target plates and the edge transport characteristics of W impurities. The combined effects of Ne impurity seeding and drifts on W sputtering flux ($f_{\mathrm{s,W}}$) are assessed through external calculations utilizing target plasma conditions provided by SOLPS-ITER. In detail, $f_{\mathrm{s,W}}$ is expressed as [25, 27, 55–58]:

$$f_{s,\mathrm{W}} = f_{\mathrm{ion}} . Y_{\mathrm{W,phys}} \tag{4}$$

$$Y_{\mathrm{W,phys}}(E_0) = QS_n(\epsilon)\left[1-\left(\frac{E_{\mathrm{th}}}{E_0}\right)^{2/3}\right]\left(1-\frac{E_{\mathrm{th}}}{E_0}\right)^{2} \times (\cos\theta)^{-\xi}\exp\left\{\xi\left[1-(\cos\theta)^{-1}\right]\right\}\cos\theta_{\mathrm{opt}} \tag{5}$$

where $Y_{\mathrm{W,phys}}$, E_0, E_{th}, Q and S_n are the W impurity sputtering yield, incident energy, threshold energy, yield factor, and nuclear stopping cross section, respectively, and θ is the incident angle which is assumed to be an average of 45° by referring to [26]. Besides, ξ and θ_{opt} are fitting parameters. The parameter f_{ion} represents the particle flux corresponding to each charge state of the bombarding species. As described in section 2, contributions to W sputtering from D, Ne, and W species are considered. However, the contribution of D species to W sputtering is negligible. This is attributed to the relatively high threshold energy for W sputtering by D (∼228.84 eV) [57] and the low incident energy [59] of D^{+} ions on the target plates, which is determined by the electron and ion temperatures and remains below 155 eV in the simulations.

The typical target profiles of W sputtering flux under varying $\Gamma_{\mathrm{Ne,puff}}$ for the three simulated scenarios are presented in figure 21. The results demonstrate that both the $\Gamma_{\mathrm{Ne,puff}}$ and drift effects significantly influence W sputtering. Compared to the main ions, Ne impurity ions exhibit a relatively higher mass, which results in a lower threshold energy (E_{th}) for sputtering, and possess higher incident energy that is dependent on their charge state [59]. While Ne puffing can reduce the physical sputtering yield of W by cooling the divertor plasma, the significantly increased bombardment flux of Ne species (f_{ion}) can markedly enhance the W sputtering flux. Consequently, W sputtering from the target may not be effectively mitigated and could instead be substantially amplified. In drift-free scenarios, as described in section 3.1, target plasma temperatures in the far SOL remains relatively high (typically $T_{\mathrm{e}} > 10$ eV) even at high $\Gamma_{\mathrm{Ne,puff}}$ (figures 5 and 7). This results in W sputtering flux profiles that are more peaked in the far SOL, particularly at high $\Gamma_{\mathrm{Ne,puff}}$ (figure 21). The inclusion of drifts modulates the target W sputtering flux by altering particle flux (f_{ion}) and energy (E_0) of the incident species. Specifically, in full-drift scenarios with upward ion $\boldsymbol{B}\times\nabla B$ drift, the W sputtering flux magnitudes at the UI and LO targets are significantly lower (mainly due to the lower plasma temperature) than those at the LI and UO targets. Furthermore, the W sputtering

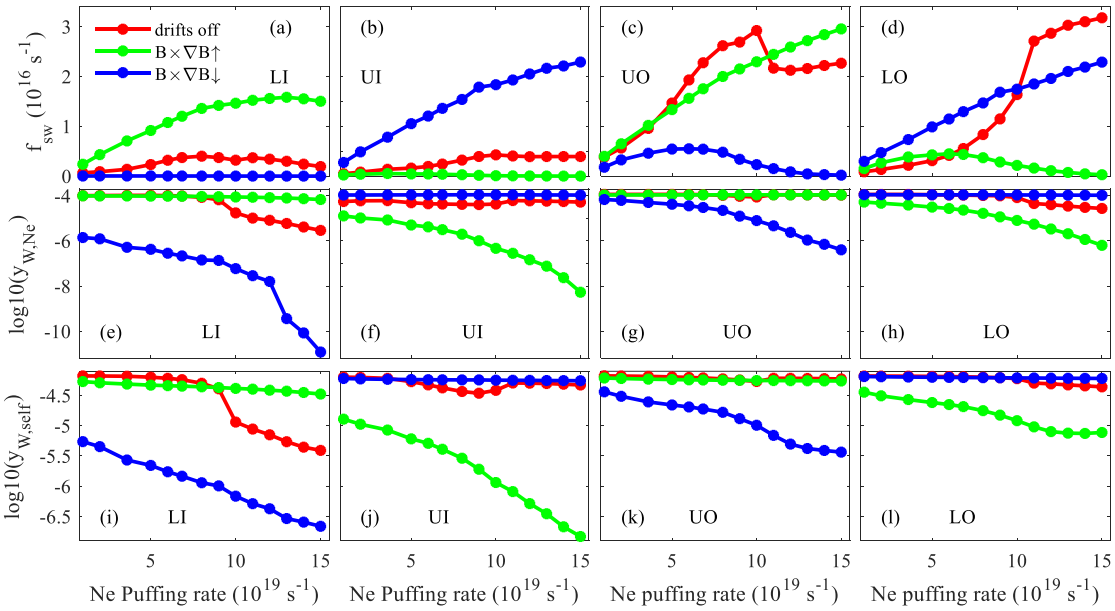

Figure 22. Integrated W impurity sputtering flux and effective W sputtering yields by Ne and W species plotted against $\Gamma_{\mathrm{Ne,puff}}$ for three simulated scenarios at various target plates.

flux profiles at the UI and LO target plates exhibit pronounced peaks near the separatrix, while those at the LI and UO target plates display a relatively broader distribution. Similarly, the reversal of ion $\boldsymbol{B}\times\nabla B$ drift direction from upward to downward leads to significantly smaller and more peaked (near the separatrix) W sputtering flux at the LI and UO target plates, while resulting in much larger and broader W sputtering flux at the LO and UI target plates.

Analysis of figures 7 and 22 reveals at the target plates where $T_{\mathrm{e,peak}}$ exceeds 10 eV, the sputtering yields for both Ne and W—defined as the ratio of the total W sputtering flux to the total incident flux of the bombarding species (summed over all the charge states)—remain largely unchanged (on the order of 10^{-4}) with increasing $\Gamma_{\mathrm{Ne,puff}}$. Under these high-temperature conditions, the W sputtering flux at the target plates is governed by the incident particle flux and thus increases with $\Gamma_{\mathrm{Ne,puff}}$. As $\Gamma_{\mathrm{Ne,puff}}$ increases further, a significant reduction in both W sputtering yield and flux occurs only when $T_{\mathrm{e,peak}}$ falls below 10 eV. Due to the limited radiative cooling enhancement from Ne seeding, in divertor plasmas with low far-SOL radial particle transport (section 3.1), increasing $\Gamma_{\mathrm{Ne,puff}}$ does not substantially reduce the integrated W sputtering flux. However, the observed saturation of the W flux at higher $\Gamma_{\mathrm{Ne,puff}}$ suggests that exceeding the maximum simulated puffing rate (1.5×10^{20} s^{-1}) could lead to effective suppression. Furthermore, comparisons between drift scenarios show that at low $\Gamma_{\mathrm{Ne,puff}}$ ($\Gamma_{\mathrm{Ne,puff}}\leqslant 6.0\times10^{19}$ s^{-1}), the no-drift case exhibits a lower total W sputtering flux—attributed to its lower Ne divertor content (section 3.2). At high $\Gamma_{\mathrm{Ne,puff}}$ ($\Gamma_{\mathrm{Ne,puff}}>6.0\times10^{19}$ s^{-1}), the no-drift case exhibits a higher sputtering flux, as $T_{\mathrm{e,peak}}$ at the LO, UI and UO target plates remains above 10 eV, leading to sustained high sputtering conditions.

To gain deeper insights into the transport properties of W impurities, figure 23 illustrates the typical two-dimensional distributions of the ionization source of W^+ originating from neutral W atoms ($S_W{}^+$). The relatively low first ionization energy of W atoms (~7.68 eV) leads to $S_W{}^+$ predominantly accumulating in the divertor regions near the target plates, accounting for 70%–90% of the observed distribution. The presence of $S_W{}^+$ in the main SOL is attributed to the recycling of W ions that reach the main vessel, which subsequently return to the far SOL and undergo re-ionization. In the divertor region, $S_W{}^+$ exhibits a pronounced tendency to localize in the PFR, despite the relatively low W sputtering flux in the PFR across all simulation cases (figure 21). Notably, $S_W{}^+$ is virtually absent in most of the near SOL and the core plasma region.

Figure 24 illustrates the typical W ion flow patterns within the computational domain under three simulated scenarios at $\Gamma_{\mathrm{Ne,puff}}=1.0\times10^{20}$ s^{-1}. Our investigation begins with the drift-free scenario. In this scenario, the strong $S_W{}^+$ in the PFR generates a significant W ion flux from the PFR to the CFR via the separatrix in all divertor regions. Owing to the $(1+m_D/m_{\mathrm{imp}})$ term in the friction efficient (c_{fr}) [52], the stagnation point is dependent on the impurity masses m_{imp}, shifting towards the target at higher masses. As a result, friction coefficient for Ne is about 9% larger than that for W, subtly influencing the stagnation point position. Comparing figures 15 and 24, the stagnation point for the poloidal velocity of W ($u_{\mathrm{pol,W}}$) is marginally closer to the target compared to that for $u_{\mathrm{pol,Ne}}$. W ions that undergo their first ionization above the stagnation point for $u_{\mathrm{pol,W}}$ leak from the divertor regions through the near SOL. The differing spatial distributions of $S_W{}^+$ and $S_{Ne}{}^+$ in the main SOL and core lead to distinct ion flux patterns for Ne and W in these regions. A portion of

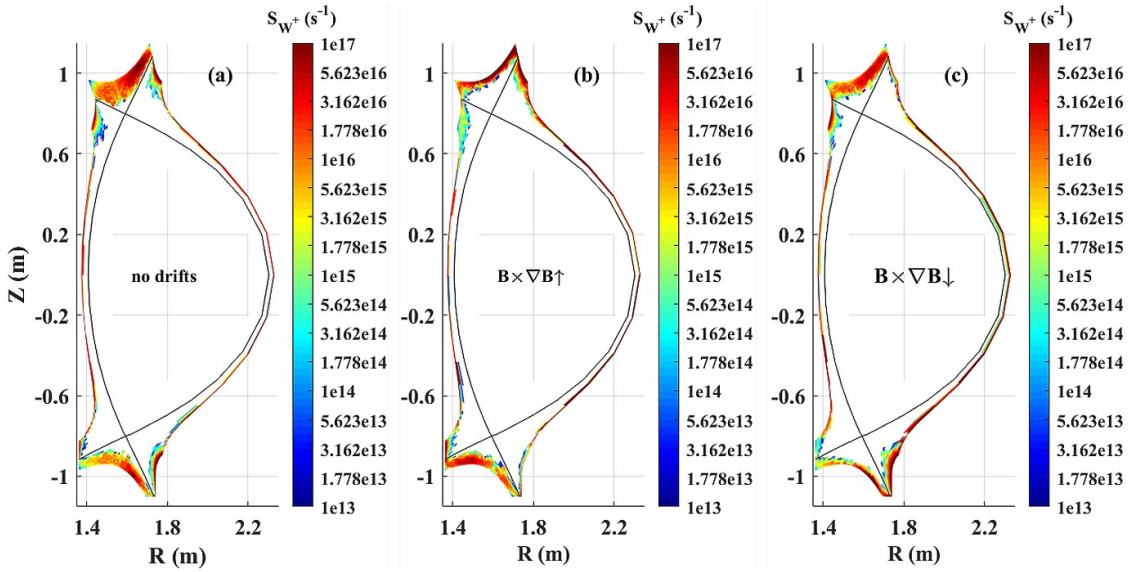

Figure 23. Two-dimensional spatial distribution of the W^+ ionization source from the neutral W atoms ($S_{W}{}^{+}$, in s^{-1}) for the three simulated scenarios at a Ne puffing rate of $\Gamma_{\mathrm{Ne,puff}} = 1.0 \times 10^{20}$ s^{-1}.

W ions in the main SOL, originating either from the divertor regions or from the ionization of W atoms in the far SOL, penetrate the core plasma via the separatrix at the LFS and extend radially inward. Within the core, W ions exhibit poloidal movement from the LFS to the HFS. Conversely, a fraction of core W ions return to the main SOL via the separatrix at both the HFS and LFS. Notably, as shown in figure 24(*a*), a strong poloidal flow near the core boundary transports W ions from the LFS to the HFS. This results in a relatively high W core density, tending to accumulate farther from the separatrix. Near the core boundary, W density is more concentrated at the HFS (figure 25). Additionally, a portion of W ions in the main SOL is transported from the near SOL to the far SOL. In the far SOL, these ions are predominantly directed toward the targets and the vacuum vessels, with only a minor fraction moving from the far SOL to the near SOL. Within the divertor regions, the W density is more concentrated in the PFR compared to the CFR, primarily due to the strong $S_{W}{}^{+}$ present in the PFR.

The inclusion of ion drifts significantly alters the W ion flow pattern across all plasma regions. Although full-drift scenarios—featuring an upward (or downward) ion B×∇B drift—generally eliminate the $u_{\mathrm{pol,W}}$ stagnation points across most LI and UO (or LO and UI) divertor regions, they concurrently shift these stagnation points for $u_{\mathrm{pol,W}}$ toward the target plate within the narrow region adjoining the separatrix. The elimination of the $u_{\mathrm{pol,W}}$ stagnation point suppresses W leakage, while its shift toward the target enhances leakage through the X-point region. Conversely, drift effects may induce stagnation points for $u_{\mathrm{pol,W}}$ in the far SOL of the LO and UI (for upward ion $\boldsymbol{B}\times\nabla B$ drift) or LI and UO (for downward ion $\boldsymbol{B}\times\nabla B$ drift) divertor regions, resulting in a marked increase in W leakage from these divertor regions. Hence, it remains challenging to demonstrate whether drifts can promote the W divertor retention. Furthermore, the inclusion of drifts in the simulations enhances the W ion flux from the far SOL to the near SOL. Depending on the direction of the ion $\boldsymbol{B}\times\nabla B$ drift (upward or downward), W ions in the main SOL primarily enter the core plasma region through the top (or bottom) portion of the separatrix at the LFS and through the bottom (or top) portion of the separatrix at the HFS, with the LFS pathway dominating over the HFS pathway. Simultaneously, depending on the direction of the ion $\boldsymbol{B}\times\nabla B$ drift (upward or downward), a fraction of W ions in the core can return to the main SOL via the bottom (or top) portion of the separatrix at the LFS and through the top (or bottom) portion of the separatrix at the HFS. A significant portion of W ions in core cannot penetrate deeply into the region farther from the separatrix due to the relatively low inward radial flux of W ions in the near-separatrix region. Consequently, the W density in core is more concentrated near the separatrix compared to regions farther from the separatrix (figure 25). The W ion fluxes from the PFR to the CFR, driven by strong $S_{W}{}^{+}$ in the PFR, can be enhanced or disturbed by $\boldsymbol{E}\times\boldsymbol{B}$ drift-driven W ion flows. These flows transport W ions from LI/UO (LO/UO) to LO/UI (LI/UO) through the PFR for upward (downward) ion $\boldsymbol{B}\times\nabla B$ drift, further influencing W transport dynamics. Moreover, depending on the direction of ion $\boldsymbol{B}\times\nabla B$ drift (upward or downward), the W density in the bottom portion of the HFS SOL is an order of magnitude higher (or lower) than that in the top portion, and vice versa for the LFS SOL. This highlights the pronounced in-out and up-down asymmetry in W density within the (divertor and main) SOL induced by drift effects.

To meticulously investigate the influence of $\Gamma_{\mathrm{Ne,puff}}$ on the spatial distribution of W density, figure 26 illustrates the spatially averaged W density across various plasma regions as a function of $\Gamma_{\mathrm{Ne,puff}}$. From figure 26, although the total W sputtering flux from the target plates cannot be effectively

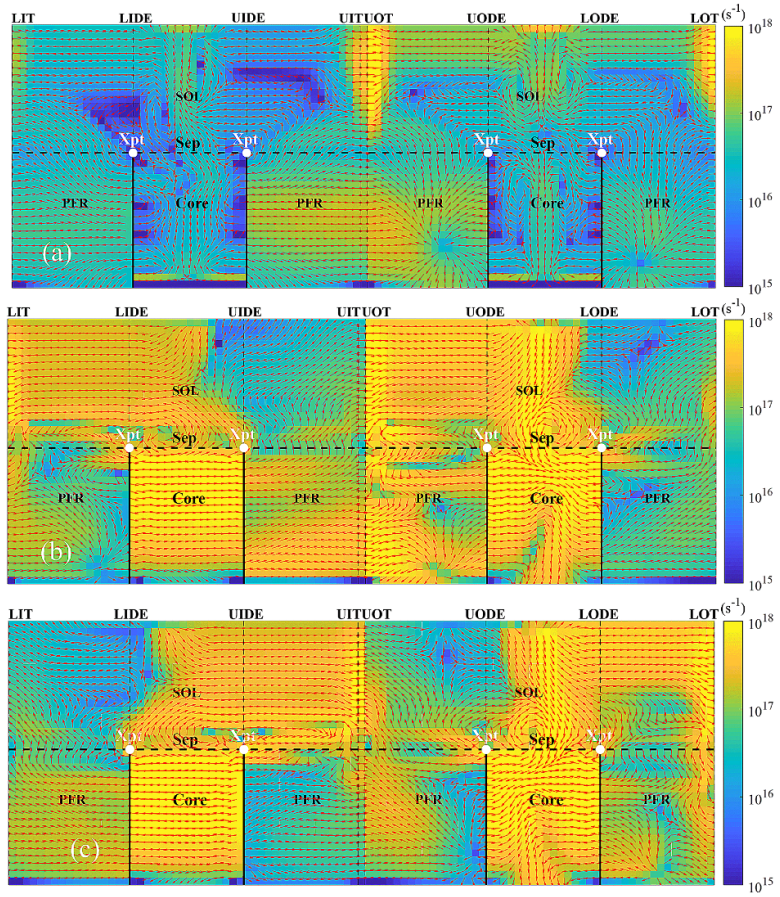

Figure 24. The two-dimensional spatial distribution of W ion flux (summed over all the charge states) within the B2.5 computational mesh at a Ne puffing rate of $\Gamma_{\mathrm{Ne,puff}} = 1.0 \times 10^{20}\ \mathrm{s}^{-1}$ for three simulated conditions: (*a*) absence of ion drift effects, (*b*) presence of full ion drifts with an upward $\boldsymbol{B}\times\nabla B$ drift ($\boldsymbol{B}\times\nabla B\uparrow$), and (*c*) presence of full ion drifts with a downward $\boldsymbol{B}\times\nabla B$ drift ($\boldsymbol{B}\times\nabla B\downarrow$). Vertical lines, from left to right, indicate the positions of the LI target plate (LIT), LI divertor entrance (LIDE), UI divertor entrance (UIDE), UI target plate (UIT), UO target plate (UOT), UO divertor entrance (UODE), LO divertor entrance (LODE), and the LO target plate (LOT).

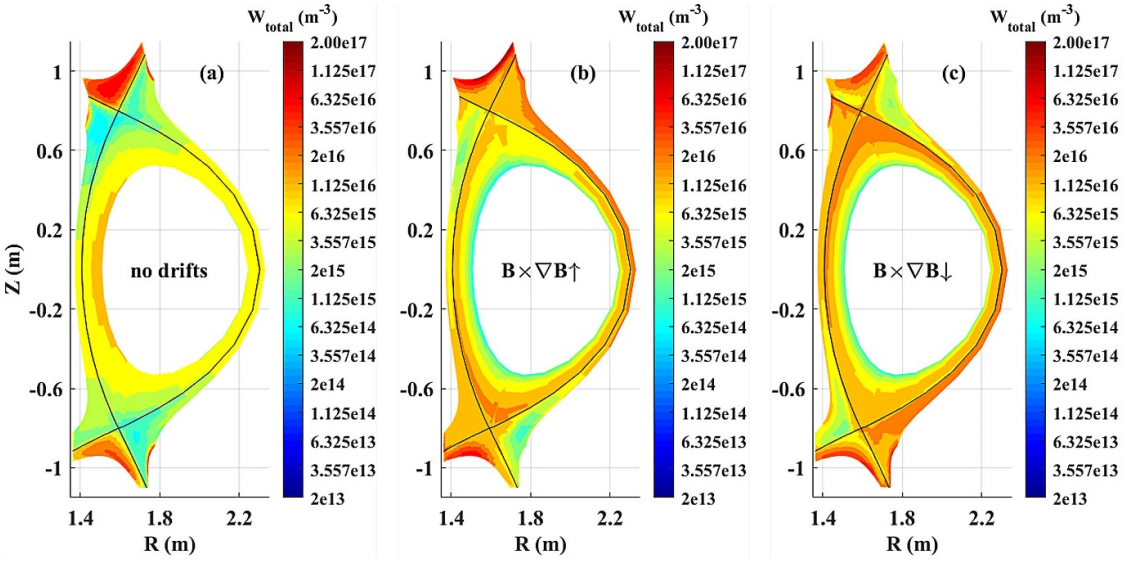

Figure 25. Two-dimensional spatial distributions of W impurity density for the three simulate scenarios at a Ne puffing rate of $\Gamma_{\mathrm{Ne,puff}} = 1.0 \times 10^{20}\ \mathrm{s}^{-1}$.

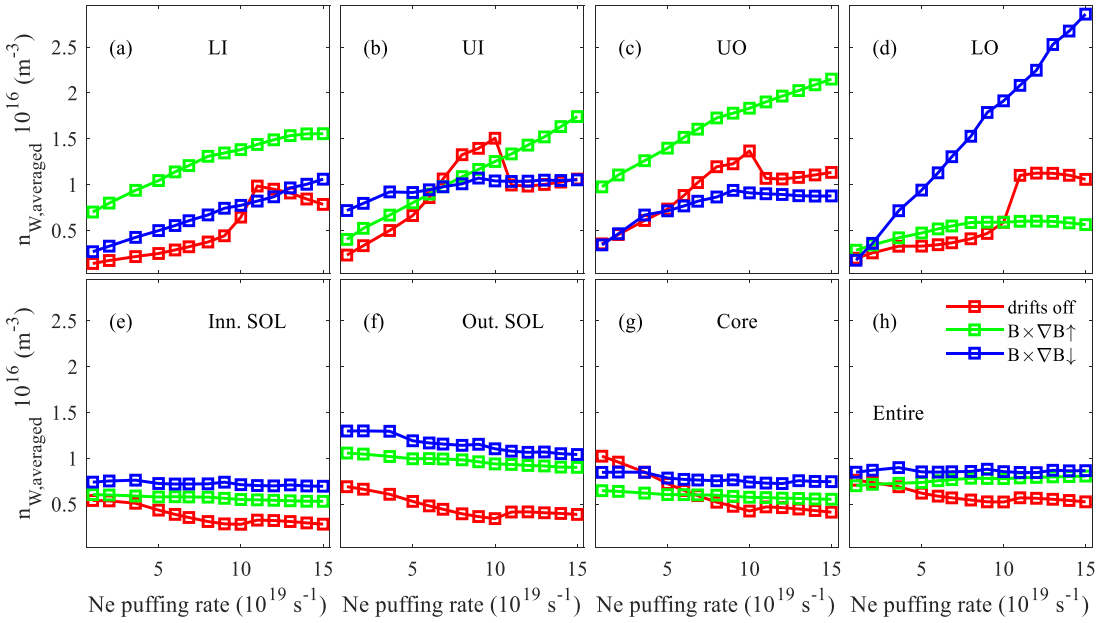

Figure 26. Spatially averaged W density in various plasma regions as a function of Ne puffing rate, including the LI, UI, UO, and LO divertor regions (*a*)–(*d*), the inner and outer SOL (*e*)–(*f*), and the core (*g*). Additionally, the spatially averaged W density for the entire computational domain is presented in panel (*h*).

mitigated by elevating the $\Gamma_{\mathrm{Ne,puff}}$ (figure 22), W density in the upstream regions, including the main SOL and core, demonstrates a decreasing trend. This reduction is attributed to the diminished ratio of thermal force and friction coefficient ($\frac{F_{th}}{c_{fr}}$) (refer to equation (3)) due to enhanced radiative cooling effects. Conversely, W density within the divertor regions exhibits an increasing trend with higher $\Gamma_{\mathrm{Ne,puff}}$. However, in no-drift scenarios, the redistribution of Ne density from the upper to the lower divertor regions via the main SOL significantly influences W density within the divertor regions, underscoring the complex interplay between Ne seeding and W transport dynamics.

For full-drift scenarios with an upward ion $\boldsymbol{B}\times\nabla B$ drift, increasing $\Gamma_{\mathrm{Ne,puff}}$ leads to a decrease in the net W ion flux entering both the LI and UO divertor regions (figure 27). However, a significant increase in $S_{\mathrm{W}}{}^{+}$ is observed in these regions: from 4.3×10^{18} s^{-1}–1.1×10^{19} s^{-1} in the LI divertor, and from 2.5×10^{19} s^{-1}–5.5×10^{19} s^{-1} in the UO divertor. Consequently, W density in both divertor regions increases notably with rising $\Gamma_{\mathrm{Ne,puff}}$ (figure 26). In the UI divertor region, although $S_{\mathrm{W}}{}^{+}$ is relatively low (ranging from 7.0×10^{17} s^{-1}–2.8×10^{18} s^{-1}), the substantial transport of W ions from the UO divertor region via the PFR results in a relatively high rate of W density increase as $\Gamma_{\mathrm{Ne,puff}}$ increases. In contrast, the relatively low net flux of W ions into the LO divertor region, combined with its $S_{\mathrm{W}}{}^{+}$ being less than 4.0×10^{18} s^{-1}, leads to a relatively low W density in this region.

For full-drift scenarios with a downward ion $\boldsymbol{B}\times\nabla B$ drift, the spatial distribution of W density is also significantly modulated by the magnitude of $S_{\mathrm{W}}{}^{+}$ and the W ion fluxes through test surfaces P1 to P6. Notably, the integrated $S_{\mathrm{W}}{}^{+}$ levels in both the LI and UO divertor regions remain relatively modest, with values below 1.3×10^{18} s^{-1} and 6.5×10^{18} s^{-1}, respectively. However, the accumulation of $S_{\mathrm{W}}{}^{+}$ sources in the lower PFR, combined with the enhanced W ion transport from the LO to LI divertor region via the PFR, leads to a pronounced increase in W density within the PFR (figure 25) and (*a*) progressive rise in the averaged W density of the LI divertor region as $\Gamma_{\mathrm{Ne,puff}}$ increases (figure 26). Similarly, $S_{\mathrm{W}}{}^{+}$ in the upper PFR, along with W ion transport from the UI to UO divertor region through the PFR, contribute to elevated W density in the PFR of the UO divertor region. In the UI divertor region, $S_{\mathrm{W}}{}^{+}$ increases gradually (from 7.7×10^{18} s^{-1}–1.5×10^{19} s^{-1}), accompanied by a slow rise in W density due to the reduction in net W ion flux entering this region. Importantly, despite the decreasing net W ion flux into the LO divertor region, the $S_{\mathrm{W}}{}^{+}$ in this region exhibits significantly higher values (ranging from 1.98×10^{19} s^{-1}–4.18×10^{19} s^{-1}) and increases rapidly with $\Gamma_{\mathrm{Ne,puff}}$, resulting in a marked elevation of W density within the LO divertor region.

Figure 28 illustrates W divertor retention and core leakage characteristics. The W divertor retention is defined as the ratio of total W particles in the lower/upper divertor to the total in the computational domain, while W core leakage is characterized by the ratio of W particles in the core plasma region to the total. Both metrics exhibit strong dependencies on Ne seeding levels and drift effects. Simulations indicate that in CDN plasmas, as in SN configurations [28], W core leakage decreases with increasing $\Gamma_{\mathrm{Ne,puff}}$, particularly at lower $\Gamma_{\mathrm{Ne,puff}}$ values, which benefits sustained high-performance plasma operations on EAST. Furthermore, W divertor retention is consistently higher under upward ion $\boldsymbol{B}\times\nabla B$ drift compared to downward

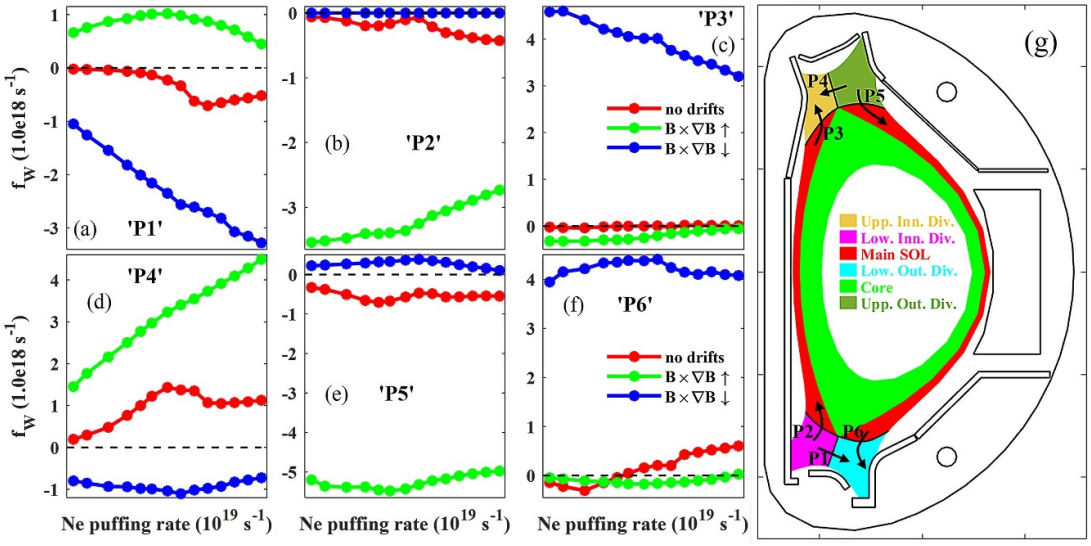

Figure 27. The integrated poloidal W ion flux transversing the test surfaces P1–P6 (*a*)–(*f*) is presented, with the positive directions of these fluxes indicated by arrows in panel (*g*).

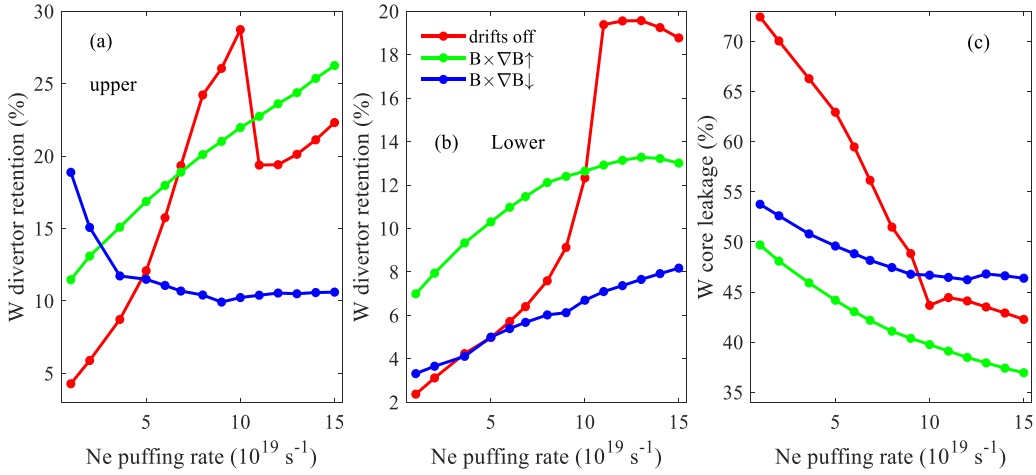

Figure 28. Retention of W impurity in the upper (*a*) and lower (*b*) divertors together with the core leakage of W impurity for the three simulated scenarios plotted as a function of Ne puffing rate.

drift as $\Gamma_{\mathrm{Ne,puff}}$ increases. Similarly, W core leakage is systematically lower for upward drift. Furthermore, across all simulations, W accounts for only a minor fraction of the total radiative power loss, with values ranging from 0.140 to 0.287 MW. These findings demonstrate significant implications for controlling W core accumulation in EAST plasmas.

4. Conclusions

Impurity seeding is an essential strategy for future tokamak fusion reactors, such as ITER, to effectively mitigate peak heat flux and temperature at the divertor target plates. However, addressing the challenges of core plasma contamination and excessive target material erosion caused by impurity seeding remains a critical unresolved issue. In this study, the comprehensive edge modeling code package SOLPS-ITER was employed to simulate Ne-seeded EAST plasmas under the CDN configuration. The investigation focused on the combined effects of fluid drifts and Ne impurity seeding level on Ne impurity transport and on the production and transport properties of W impurities. This was achieved by analyzing the ionization sources of Ne^+ and W^+ from Ne and W atoms, as well as the stagnation points for the poloidal velocity of Ne and W in various scenarios. Prior to this, the impacts of drifts and Ne seeding on divertor plasma conditions were systematically examined.

Our simulation results reveal that, in the drift-free scenario, the radial particle transport in the far SOL is significantly suppressed, leading to limited plasma and impurity ion transport from the near SOL to the far SOL. Consequently, the plasma density (n_e) in the far SOL remains remarkably low. This, in turn, results in temperature peaks ($T_{\mathrm{e,peak}}$) predominantly localized in the far SOL, which are highly resistant to reduction through increased Ne impurity seeding level. The main (D^+) ions exhibit a strong preference for transport from the LO and

UO divertor regions to the LI and UI divertor regions via the PFR. This transport pattern is driven by the relatively intense ionization source of D^+ ($S_D{}^+$) in the LO and UO divertor regions compared to the LI and UI divertor regions. The inclusion of drift effects significantly alters particle transport characteristics in the divertor regions. Specifically, the upward ion $\boldsymbol{B}\times\nabla B$ drift reduces the radial D^+ ion transport in the near SOL of the LI and UO divertor regions, even reversing the radial D^+ flux crossing the separatrix in these regions from the CFR to the PFR. This pronounced transport of D^+ ions from the LI/UO divertor region to the LO/UI divertor region via the PFR leads to a substantial decrease in n_e values at the LI and UO target plates. Furthermore, the reduction of n_e near the separatrix causes the T_e peaks to shift from the far SOL to the near SOL adjacent to the separatrix. In contrast, the $\boldsymbol{E}\times\boldsymbol{B}$ drift enhances radial particle transport in the LO and UI divertor regions, resulting in a significant increase in n_e values in the far SOL and a corresponding decrease in n_e in the near SOL and PFR. This redistribution effectively shifts the n_e (T_e) peak outward (inward) from the near (far) SOL to the far (near) SOL. Consequently, the T_e values at the LO and UI target plates become more responsive to reductions through increased Ne seeding rates. Notably, reversing the direction of the ion $\boldsymbol{B}\times\nabla B$ drift from upward to downward leads to a marked decrease in n_e values at the LO and UI target plates. Simultaneously, this reversal causes an outward (inward) shift of the n_e (T_e) peak from the near (far) SOL to the far (near) SOL at the LI and UO target plates.

In drift-free scenarios, the poloidal plasma ion (D^+) flows through the PFR and SOL are primarily driven by the ionization source of D^+ ($S_\mathrm{D}{}^+$) in the divertor regions, which is significantly influenced by Ne impurity seeding. At relatively low Ne seeding rates, $S_\mathrm{D}{}^+$ in the upper (UI and UO) divertor regions is larger than in the lower (LI and LO) divertor regions. However, at higher Ne seeding rates, $S_\mathrm{D}{}^+$ in the lower divertor regions becomes comparable to or even exceeds that in the upper divertor regions, leading to an inversion of the background plasma ion flow through the SOL and a redistribution of Ne particle density—from the upper divertor to the main SOL, and from the main SOL to the lower divertor. Furthermore, in the drift-free scenario, increasing the Ne seeding rate results in a significant displacement of the stagnation point for the poloidal velocity of Ne, moving it farther away from the target plates. This reduces Ne leakage from the divertor. Another critical factor influencing the Ne density distribution across the computational domain is the ionization source of Ne^+ ions ($S_\mathrm{Ne}{}^+$) from neutral Ne atoms. In the drift-free scenario, $S_\mathrm{Ne}{}^+$ is strongest in the core plasma region, enabling a large fraction of Ne ions to be transported radially into the core boundary farther from the separatrix. Consequently, Ne density in the core plasma region is significantly higher and is more concentrated near the core boundary compared to regions near the separatrix. Notably, increasing the Ne seeding level reduces the proportion of $S_\mathrm{Ne}{}^+$ in the core, which also decreases the proportion of Ne particles in the core plasma region. The inclusion of drift effects in the simulations reveals that the $\boldsymbol{E}\times\boldsymbol{B}$ drift plays a dominant role in determining the poloidal impurity ion flow. In full-drift scenarios, the stagnation point for the poloidal velocity of Ne becomes much less sensitive to increases in the Ne seeding rate, and the divertor leakage of Ne impurities decreases only gradually as the Ne seeding rate rises. Additionally, in full-drift scenarios, $S_\mathrm{Ne}{}^+$ in the core is significantly lower than in the drift-free scenario. The Ne ions in the core are more concentrated near the separatrix due to the strong poloidal plasma rotation and relatively weak radial Ne particle transport in this region.

The W sputtering flux is governed by the target plasma parameters, which can be significantly modified by both drift effects and Ne impurity seeding. In the drift-free scenario, the W sputtering flux from the far SOL is substantial and cannot be effectively mitigated by increasing the Ne seeding level due to limited plasma and Ne impurity ion transport from the near SOL to the far SOL. Additionally, the redistribution of Ne density at relatively high Ne puffing rate influences the W sputtering flux at the target plates. In the full-drift simulations, the W sputtering yield at the target plates can be suppressed by increasing the Ne seeding level, but only when the radial particle transport into the far SOL of the divertor region is significantly enhanced by the $\boldsymbol{E}\times\boldsymbol{B}$ drift. Consequently, for upward ion $\boldsymbol{B}\times\nabla B$ drift, the W sputtering yield at the LI and UO target plates cannot be effectively reduced, whereas for downward ion $\boldsymbol{B}\times\nabla B$ drift, the W sputtering yield at the LO and UI target plates cannot be significantly decreased, even with increased Ne seeding levels. The ionization source of W^+ ions ($S_\mathrm{W}{}^+$) from neutral W atoms tends to be localized in the divertor regions, with negligible $S_\mathrm{W}{}^+$ observed in the core plasma across all simulation cases. The W core leakage decreases with increasing $\Gamma_\mathrm{Ne,puff}$, particularly at relatively low $\Gamma_\mathrm{Ne,puff}$ values, which is beneficial for maintaining high-performance plasma operations on EAST. Furthermore, the W divertor retention consistently exhibits higher values for upward ion $\boldsymbol{B}\times\nabla B$ drift compared to downward ion $\boldsymbol{B}\times\nabla B$ drift. Similarly, the W core leakage also shows systematically lower values for upward ion $\boldsymbol{B}\times\nabla B$ drift relative to the downward case.

Our analysis confirms that the divertor leakage of Ne and W impurities in CDN plasmas is governed by the same ionization-front and stagnation-point mechanisms previously identified in SN configurations [33], with this leakage being progressively suppressed as $\Gamma_\mathrm{Ne,puff}$ increases. Comparative full-drift simulations [53] indicate that at elevated $\Gamma_\mathrm{Ne,puff}$, the CDN configuration yields a comparatively weaker enhancement in divertor Ne retention and a less substantial reduction in core Ne leakage. The dynamics of plasma flows in both the SOL and PFR are underscored as critical to the observed divertor asymmetry and impurity transport. Moreover, the in-out asymmetry in T_e within CDN plasmas exhibits a dependence on $\Gamma_\mathrm{Ne,puff}$ that is distinct from that seen in SN configurations [53]. These results enhance our understanding of impurity-seeded plasmas and their impact on tungsten behavior in the EAST tokamak, offering insights of relevance to ITER and future fusion reactors. Further experimental validation is planned to confirm the simulated trends.

Acknowledgment

This work was sponsored by the National Natural Sciences Foundation of China (Nos. 12075052, 12175034 and 12275098), the Open Fund of Magnetic Confinement Fusion Laboratory of Anhui Province (Grant No. 2024AMF04001), and the Fundamental Research Funds for the Central Universities (Nos. 232024G-10 and 2232025G-10). We thank the staff members at EAST (https://cstr.cn/31130.02.EAST), for providing technical support and assistance in data collection and analysis.

ORCID iDs

Fuqiong Wang 0000-0003-0145-5931
Y.F. Xu 0000-0003-2960-9488
S.C. Liu 0000-0002-7298-0680
F.C. Zhong 0000-0002-4038-4040
Y. Liang 0000-0002-9483-6911

References

[1] Stangeby P.C. 2000 *The Plasma Boundary of Magnetic Fusion Devices* (Institute of Physics Publishing)
[2] Naujoks D. *et al* 1996 *Nucl. Fusion* **36** 671–87
[3] Loarte A. *et al* 2007 *Nucl. Fusion* **47** S203–63
[4] Pitts R.A. *et al* 2011 *J. Nucl. Mater.* **415** S957–64
[5] Wischmeier M. 2015 *J. Nucl. Mater.* **463** 22–29
[6] Gunn J.P. *et al* 2017 *Nucl. Fusion* **57** 046025
[7] Kallenbach A. *et al* 2013 *Plasma Phys. Control. Fusion* **55** 124041
[8] Ioki K. *et al* 1998 *J. Nucl. Mater.* **258–263** 74–84
[9] Gerald P. *et al* 2022 *Fusion Eng. Des.* **174** 112994
[10] Kallenbach A. *et al* 2011 *J. Nucl. Mater.* **415** S19–S26
[11] Matthew S.P. *et al* 2024 *Nucl. Fusion* **64** 096030
[12] Neu R. *et al* 2002 *Plasma Phys. Control. Fusion* **44** 811–26
[13] Umansky M.V. *et al* 2010 *Contrib. Plasma Phys.* **50** 350–5
[14] Piras F., Coda S., Duval B.P., Labit B., Marki J., Medvedev S.Y., Moret J.-M., Pitzschke A. and Sauter O. 2010 *Phys. Rev. Lett.* **105** 155003
[15] Valanju P.M., Kotschenreuther M. and Mahajan S.M. 2010 *Fusion Eng. Des.* **85** 46–52
[16] Herrmann A. 2002 *Plasma Phys. Control. Fusion* **44** 883
[17] Meyer H. *et al* 2006 *Nucl. Fusion* **46** 64
[18] Brunner D. *et al* 2018 *Nucl. Fusion* **58** 076010
[19] Ambrosino R., Castaldo A., Ha S., Loschiavo V.P., Merriman S. and Reimerdes H. 2019 *Fusion Eng. Des.* **146** 2717
[20] Gong X. *et al* 2024 *Nucl. Fusion* **64** 112013
[21] Xu G.S. *et al* 2021 *Nucl. Fusion* **61** 126070
[22] Xu G.S. *et al* 2020 *Nucl. Fusion* **60** 086001
[23] Wang F., Liang Y., XU Y., Zha X., Zhong F., Mao S., Duan Y. and HU L. 2023 *Plasma Sci. Technol.* **25** 115102
[24] He T. *et al* 2024 *Phys. Plasmas* **31** 042512
[25] Zhao X., McFadden G.B. and Cerfon A.J. 2020 *Plasma Phys. Control. Fusion* **62** 055015
[26] GAO Shanlu et al 2022 *Plasma Sci. Technol.* **24** 075104
[27] Wang Y. *et al* 2021 *Plasma Phys. Control. Fusion* **63** 085002
[28] Wang Y. *et al* 2023 *Nucl. Fusion* **63** 096024
[29] Xu G. *et al* 2024 *Nucl. Fusion* **64** 126048
[30] Wiesen S. *et al* 2015 *J. Nucl. Mater.* **463** 480–4
[31] Bonnin X., Dekeyser W., Pitts R., Coster D., Voskoboynikov S. and Wiesen S. 2016 *Plasma Fusion Res.* **11** 1403102
[32] Rozhansky V., Molchanov P., Veselova I., Voskoboynikov S., Kirk A. and Coster D. 2012 *Nucl. Fusion* **52** 103017
[33] Senichenkov I.Y., Kaveeva E.G., Sytova E.A., Rozhansky V.A., Voskoboynikov S.P., Veselova I.Y., Coster D.P., Bonnin X. and Reimold F. 2019 *Plasma Phys. Control. Fusion* **61** 045013
[34] Nichols J.H. *et al* 2021 *Nucl. Fusion* **61** 096018
[35] Toma M., Bonnin X., Sawada Y., Homma Y., Hatayama A., Hoshino K., Coster D. and Schneider R. 2013 *J. Nucl. Mater.* **438S** 620–4
[36] Rozhansky V., Kaveeva E., Molchanov P., Veselova I., Voskoboynikov S. and Coster D.C. 1994 **50** 3033–40
[37] Reiter D., Baelmans M. and Börner P. 2005 *Fusion Sci. Technol.* **47** 172
[38] Braginskii S.I. 1965 *Reviews of Plasma Physics* ed M.A Leontovich (Consultants Bureau) p 205
[39] Eckstein W. *et al* 1993 *Sputtering Data* (Max-Planck-Institut für Plasmaphysik)
[40] Gao S., Liu X., Deng G., Ming T., Li G., Zhang X., Tao Y. and Gao X. 2021 *AIP Adv.* **11** 025233
[41] Zhdanov V. 2002 *Transport Processes in Multicomponent Plasma* (Taylor & Francis)
[42] Sytova E., Coster D., Senichenkov I., Kaveeva E., Rozhansky V., Voskoboynikov S., Veselova I. and Bonnin X.P. 2020 *Phys. Plasmas* **27** 082507
[43] Makarov S.O., Coster D.P., Rozhansky V.A., Stepanenko A.A., Zhdanov V.M., Kaveeva E.G., Senichenkov I.Y. and Bonnin X. 2021 *Phys. Plasmas* **28** 062308
[44] Makarov S.O., Coster D.P., Rozhansky V.A., Voskoboynikov S.P., Kaveeva E.G., Senichenkov I.Y., Stepanenko A.A., Zhdanov V.M. and Bonnin X. 2021 *Contrib. Plasma Phys.* **62** e202100165
[45] Makarov S.O., Coster D.P., Kaveeva E.G., Rozhansky V.A., Senichenkov I.Y., Veselova I.Y., Voskoboynikov S.P., Stepanenko A.A., Bonnin X. and Pitts R.A. 2023 *Nucl. Fusion* **63** 026014
[46] Kaveeva E., Rozhansky V., Senichenkov I., Veselova I., Voskoboynikov S., Sytova E., Bonnin X. and Coster D. 2018 *Nucl. Fusion* **58** 126018
[47] Hu Q.S., Yao D.M., Luo G.N., Xie H., Xu C.S., Li J.G. and Wang X.M. 2010 *Fusion Eng. Des.* **85** 1508
[48] Yu Y.W. *et al* 2019 *Nucl. Fusion* **59** 126036
[49] Jia G. *et al* 2022 *Nucl. Fusion* **62** 056005
[50] Fundamenski W. 2005 *Plasma Phys. Control. Fusion* **47** R163–208
[51] Owen L.W., Canik J.M., Groebner R.J., Callen J.D., Bonnin X. and Osborne T.H. 2010 *Nucl. Fusion* **50** 064017
[52] Hitzler F., Wischmeier M., Reimold F. and Coster D.P. 2020 *Plasma Phys. Control. Fusion* **62** 085013
[53] Wang F. *et al* 2023 *Plasma Sci. Technol.* **25** 115102
[54] Neuhauser J., Schneider W., Wunderlich R. and Lackner K. 1984 *Nucl. Fusion* **24** 39–47
[55] Yamamura Y., Itikawa Y. and Itoh N. 1983 *Angular Dependence of Sputtering Yields of Monatomic Solids Report Number IPPJ-AM-26* (Institute of Plasma Physics Nagoya University)
[56] Eckstein W. 1997 *J. Nucl. Mater.* **248** 1–8
[57] Warrier M., Schneider R. and Bonnin X. 2004 *Comput. Phys. Commun.* **160** 46
[58] Eckstein W. 2008 *Vacuum* **82** 930
[59] Wang F. *et al* 2018 *Plasma Phys. Control. Fusion* **60** 125005